Highlights

Rendezvous in cislunar halo orbits: Hardware-in-the-loop simulation with coupled orbit and attitude dynamics

Vivek Muralidharan, Mohatashem Reyaz Makhdoomi, Kuldeep Rambhai Barad, Lina María Amaya-Mejía, Kathleen C. Howell, Carol Martinez, Miguel Olivares-Mendez

- Coupled orbit and attitude dynamics for rendezvous in cislunar space.

- Two-layer guidance and control algorithm; ArUco markers for vision-based navigation.

- Proof-of-concept hardware-in-the-loop validation of rendezvous in halo orbits.

- Robot Operating System (ROS) to integrate controller, robot, and pose estimator.

Rendezvous in cislunar halo orbits: Hardware-in-the-loop simulation with coupled orbit and attitude dynamics

Vivek Muralidharan[a,*], Mohatashem Reyaz Makhdoomi[a], Kuldeep Rambhai Barad[a], Lina María Amaya-Mejía[a], Kathleen C. Howell[b], Carol Martinez[a] and Miguel Olivares-Mendez[a]

[a]*Space Robotics Research Group, Interdisciplinary Centre for Security, Reliability and Trust (SnT), University of Luxembourg, L-1855 Luxembourg*
[b]*School of Aeronautics and Astronautics, Purdue University, West Lafayette, IN 47907, USA*

ABSTRACT

Space missions to Near Rectilinear Halo Orbits (NRHOs) in the Earth-Moon system are upcoming. A rendezvous technique in cislunar space is proposed in this investigation, one that leverages coupled orbit and attitude dynamics in the Circular Restricted Three-body Problem (CR3BP). An autonomous Guidance, Navigation and Control (GNC) technique is demonstrated in which a chaser spacecraft approaches a target spacecraft in a sample southern 9:2 synodic-resonant L2 NRHO, one that currently serves as the baseline for NASA's Gateway. A two-layer guidance and control approach is contemplated. First, a nonlinear optimal controller identifies an appropriate baseline rendezvous path for guidance, both in position and orientation. As the spacecraft progresses along the pre-computed baseline path, navigation is performed through optical sensors that measure the relative pose of the chaser relative to the target. A Kalman filter processes these observations and offers state estimates. A linear controller compensates for any deviations identified from the predetermined rendezvous path. The efficacy of the GNC technique is tested by considering a complex scenario in which the rendezvous operation is conducted with an uncontrolled tumbling target. Hardware-in-the-loop laboratory experiments are conducted as a proof-of-concept to validate the guidance algorithm, with observations supplemented by optical navigation techniques.

1. Introduction

The ongoing Cislunar Autonomous Positioning System Technology Operations and Navigation Experiment (CAPSTONE) mission and NASA's planned Gateway mission are to be established along a Near Rectilinear Halo Orbit (NRHO) in cislunar space [1]. The growing interest in exploring cislunar space for various scientific reasons offers opportunities to test and advance rendezvous operations, thereby improving the sustainability of such missions. The Gateway, for example, is currently being developed as a long-lasting modular space hub, offering potential human residence beyond the International Space Station (ISS). The Gateway is further expected to serve as a testing station for systems and equipment and offers logistical support for various future missions to Mars and beyond [2]. Consequently, life-support systems for the crew, essential pressurized and unpressurized cargo, supplies, fuel, and advanced external robotics equipment for science experiments will be transported and exchanged periodically. The Gateway facility is planned to contain several docking ports for visiting modules, as well as space for scientific apparatus and stowage [3]. Further, CubeSat-sized vehicles such as CAPSTONE will frequent operations in cislunar space supporting the less-risky, inexpensive and large-scale applications that can be exercised with the use of such smallsats. With activities in cislunar space becoming extensive, precise rendezvous and docking techniques become essential.

A complete architecture is proposed for the guidance, navigation and control (GNC) algorithm, and its compatibility with a real-world application is validated via hardware-in-the-loop experiments in the ZeroG-Lab facility at the University of Luxembourg. Scaled mockups of CubeSats are mounted at the end-effectors of two robotic manipulators, and the trajectory and attitude motion in cislunar environment are imparted to the robots' end-effectors. In addition, optical sensors in the form of a monocular camera mounted on the chaser spacecraft identify semantic features on the target spacecraft in actual time. Using the correspondence of the detected keypoints in the known wireframe model of the target, an Efficient Perspective-n-Point (EPnP) solver estimates the relative pose of the target. A hardware-in-the-loop test with closed feedback is performed to validate the GNC architecture; a sample scenario represents the target spacecraft tumbling with natural gravity gradient torques. The results from the hardware-in-the-loop experiments offer proof-of-concept for utilizing optical navigation methods for planning rendezvous operations in cislunar environments, and eventually in deep space.

A coupled orbit and attitude dynamics in the Circular Restricted Three-body Problem (CR3BP) is leveraged to achieve the close proximity operations in this investigation [4–7]. The target body is considered to be stationed along the 9:2 synodic resonant southern L2 NRHO in the Earth-Moon system, comparable to the baseline trajectory for the Gateway. In this investigation, however, the target spacecraft is considered passive and does not have active controllers to change its orbit or orientation. Nonetheless, the chaser

---

*Corresponding author

✉ vivek.muralidharan@uni.lu (V. Muralidharan);
mohatashem.makhdoomi@uni.lu (M.R. Makhdoomi); kuldeep.barad@uni.lu (K.R. Barad); lina.amaya.001@student.uni.lu (L.M. Amaya-Mejía);
howell@purdue.edu (K.C. Howell); carol.martinezluna@uni.lu (C. Martinez); miguel.olivaresmendez@uni.lu (M. Olivares-Mendez)

spacecraft possesses active thrusters to deliver control maneuvers to modify its course during the rendezvous process. The effects of gravitational forces exerted by the Earth and Moon are considered for both the target and the chaser spacecraft. A two-layered guidance and control approach facilitates the close proximity operations [8]. Firstly, a nonlinear optimal controller using an Interior-Point Optimization (IPOPT) technique identifies a baseline rendezvous path for guidance, i.e., a series of setpoints in both position and orientation. Any deviations from this predetermined baseline identified through pose estimation are subsequently overcome by a linear controller. Navigation is performed using optical instruments onboard the chaser that captures the images of the target spacecraft in real-time. The procured images are subsequently processed to retrieve relative pose observations at regular intervals. The image acquisition and pose estimation process happens concurrently as the chaser spacecraft progresses towards the target. Uncertainties and sudden fluctuations in pose observations are overcome by incorporating a Kalman filter to deliver precise state estimates and run synchronously with the control algorithm [9].

This paper is organized as follows: Section 2 reviews some of the previous contributions that serve as the foundation for this investigation. Section 3 presents the equations of motion for the spacecraft in the circular restricted three-body problem, both orbit and attitude motion. Section 4 describes the computation of an optimal rendezvous path for guidance. The procedure for vision-based spacecraft navigation using pose estimation is illustrated in Section 5. The process of state estimation from filtering pose observations and determination of subsequent corrective control maneuvers to overcome deviations from the predicted path is presented in Section 6. Section 7 presents the experimental setup and the motion planning strategy for the hardware-in-the-loop experiments. Section 8 describes the experiments and lists significant results including lessons learned from the hardware-in-the-loop experiments. Finally, some important takeaways and concluding remarks are offered in Section 9.

2. Previous Contributions

There are numerous literature sources that demonstrate autonomous rendezvous in near-Earth orbit, but such unmanned autonomous operations have yet to be executed in multi-body environments [10]. Rendezvous in a multi-gravity environment is more complex and challenging due to the increased forces involved. Several researchers have explored the concept of cislunar rendezvous, particularly through trajectory planning and optimization [7, 11–15]. The inclusion of attitude dynamics becomes crucial for the final phase of the close proximity operations. With planned missions, investigations that focus on coupled orbit and attitude dynamics are upcoming [6, 10, 16, 17]. Relative navigation employing vision is drawing attention to increasing autonomy in space. Different approaches for relative spacecraft pose estimation are available in literature [18–22]. Hardware-in-the-loop tests are valuable for validating

operational feasibility and synchronizing with different subsystems, such as control algorithms, pose measurements and robotic manipulation. There are several research test beds for emulating motions in space, such as the GNC Rendezvous and Landing Simulator (GRALS) at the European Space Research and Technology Centre (ESTEC) in the Netherlands [23], the European Proximity Operations Simulator (EPOS) at the German Aeronautics Centre (DLR) [24], and the Testbed for Robotic Optical Navigation (TRON) in Stanford University [25], among others. Rendezvous in circular Earth orbits have been demonstrated at the EPOS test facility [26]. However, a comprehensive approach for integrating subsystems and in a more challenging cislunar rendezvous scenario is still limited and is the focus of current investigations.

3. Dynamics

Proximity operation in cislunar space is the point of focus. The motion of the chaser and target spacecraft for rendezvous operations are influenced by their location in cislunar space and their relative position and orientation. The dynamics for spacecraft motion are, thus, classified into three categories: (1) Evolution of the orbital motion of the target spacecraft expressed in terms of the circular restricted three-body problem for the Earth-Moon system; (2) Relative orbital motion of the chaser spacecraft relative to the target spacecraft; and (3) Attitude dynamics for both the spacecraft. For this investigation, the target spacecraft is assumed passive (no active controllers); the orbit and attitude motion evolve under natural gravitational forces and gravity torques exerted by the Earth and Moon. On the contrary, the chaser spacecraft is active; control maneuvers (external acceleration and torques) alter its trajectory and orientation.

3.1. Circular Restricted Three-Body Problem

In the case of a spacecraft in near-Earth orbits, a Keplerian solution is obtained by solving the two-body problem, which considers the gravitational force exerted on the spacecraft by a single celestial body, i.e., the Earth. Spacecrafts in cislunar region are however influenced primarily by the two main gravitational forces due to the Earth and the Moon concurrently [27]. The convenience of analytical closed-form solutions in the form of conic trajectories in the two-body problem is no longer available to describe motion in cislunar space. The circular restricted three-body problem (CR3BP) is fairly complete than the two-body problem but offers an adequate approximation for the spacecraft dynamics in the higher-fidelity model. The CR3BP offers a time-invariant motion of a spacecraft by assuming that the two primary bodies, the Earth and Moon, rotate in coplanar circular orbits about their mutual barycenter, i.e., point O [28]. The CR3BP model is expressed relative to a synodic frame [S] and rotates about the inertial frame [I] at a constant rate equal to the angular rate of revolution of the Earth and Moon. The frame [S] is defined such that the unit vector $\hat{i}_{[S]}$ points from the Earth towards the Moon, $\hat{k}_{[S]}$ is along

the positive orbital angular momentum direction, and finally, $\hat{j}_{[S]}$ completes the right-hand coordinate system. The inertial frame [I] shares the same origin as the synodic frame [S]. Figure 1 offers a schematic representation of the different coordinate frames used in this investigation. Each of the frames and their vector notation is summarized in Table 1. In the Earth-Moon system, the primary body P1 is the Earth while the Moon is represented by P2. By convention, the dynamical equations of motion for a spacecraft in the CR3BP are modeled with the position and velocity quantities non-dimensionalized using characteristic quantities. These non-dimensionalized equations offer ease for the numerical computation of trajectories in the CR3BP. Further, the characteristic length, l^*, is defined as the mean distance between the Earth and Moon, while the characteristic time, t^*, is defined as the reciprocal of the mean motion along the circular orbit of the primary bodies about their barycenter. The approximate values for characteristic length, l^*, and characteristic time t^* in the Earth-Moon system are listed in Table 2 [29]. Any dimensional quantities are retrieved by factoring in the characteristic length and time within the nondimensional quantities [30]. The orbit of interest for the rendezvous operation is in close proximity to the Moon, consequently, a Moon-centered rotating frame [M] is defined that is a direct linear translation from the [S] frame, such that,

$$x_{[M]} = (1 - \mu) - x_{[S]} \tag{1}$$

$$y_{[M]} = -y_{[S]} \tag{2}$$

$$z_{[M]} = z_{[S]} \tag{3}$$

where μ is the system mass ratio, defined as the ratio of the mass of P2 to the overall mass of the system, i.e., $\mu = m_2/(m_1 + m_2)$, where m_1 and m_2 are the masses of bodies P1 and P2, respectively. The value of μ in the Earth-Moon system is as defined in Table 2. For convenience, the dynamical equations of motion for a spacecraft in the [M] frame is expressed as

$$\ddot{x}_{[M]} - 2\dot{y}_{[M]} - x_{[M]} = -\frac{1-\mu}{d_1^3}(x_{[M]} - 1) \\ - \frac{\mu}{d_2^3}x_{[M]} - (1-\mu) \tag{4}$$

$$\ddot{y}_{[M]} + 2\dot{x}_{[M]} - y_{[M]} = -\frac{1-\mu}{d_1^3}y_{[M]} - \frac{\mu}{d_2^3}y_{[M]} \tag{5}$$

$$\ddot{z}_{[M]} = -\frac{1-\mu}{d_1^3}z_{[M]} - \frac{\mu}{d_2^3}z_{[M]} \tag{6}$$

where the quantities d_1 and d_2,

$$d_1 = \sqrt{(x_{[M]} - 1)^2 + y_{[M]}^2 + z_{[M]}^2} \tag{7}$$

$$d_2 = \sqrt{x_{[M]}^2 + y_{[M]}^2 + z_{[M]}^2} \tag{8}$$

are the scalar non-dimensional distances from the spacecraft to the primary bodies P1 and P2, respectively. These nonlinear equations of motion offer five equilibrium points (also known as Lagrange points or libration points) and an infinite number of periodic orbits are available in their neighborhood. A family of 3-dimensional periodic orbits exists near the L1 and L2 Lagrange points, commonly labeled as halo orbits [31]. In the Earth-Moon system, the 9:2 synodic resonant L2 Near Rectilinear Halo Orbit (NRHO) is the current focus for NASA's Gateway mission, and the CAPSTONE mission [1, 29]. The chosen orbit is deemed nearly stable by investigating the stability index of its monodromy matrix [32, 33]. Figure 2 offers a view of the 9:2 synodic resonant L2 NRHO in the Moon-centered rotating frame.
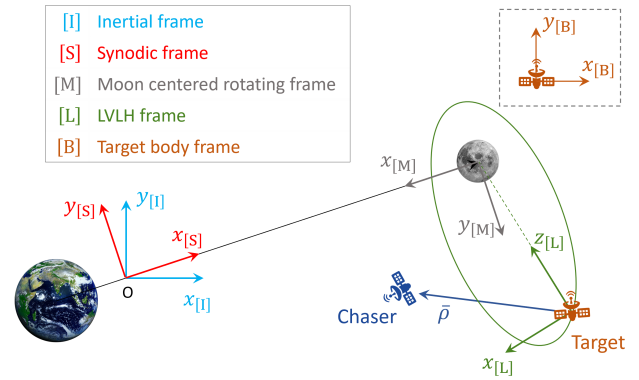

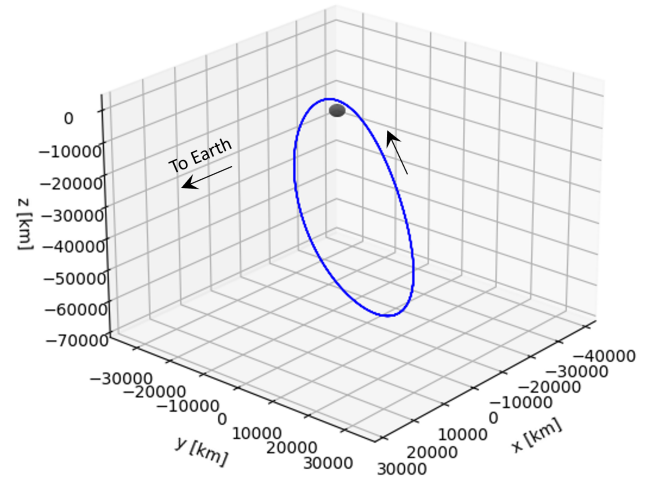**Figure 1:** Coordinate frames for spacecraft motion [16].

Figure 2: View of the 9:2 synodic resonant southern L2 NRHO in the Earth-Moon system. Plotted in [M] frame.

3.2. Relative Motion

Close proximity operations such as rendezvous are best visualized by capturing the relative dynamics between a chaser and a target spacecraft. For simplicity, a coordinate frame centered on the target spacecraft such as the Local Velocity Local Horizontal (LVLH) frame is appropriate to realize the relative motion. Frame notations are detailed in

Table 1
Frame descriptions.

Frame ID	Frame Name	Center	Unit vector notation
[I]	Inertial frame	O (Earth-Moon Barycenter)	$\hat{i}_{[I]}, \hat{j}_{[I]}, \hat{k}_{[I]}$
[S]	Synodic frame	O (Earth-Moon Barycenter)	$\hat{i}_{[S]}, \hat{j}_{[S]}, \hat{k}_{[S]}$
[M]	Moon-centered rotating frame	Moon	$\hat{i}_{[M]}, \hat{j}_{[M]}, \hat{k}_{[M]}$
[L]	Local Velocity Local Horizontal (LVLH) frame	Target spacecraft	$\hat{i}_{[L]}, \hat{j}_{[L]}, \hat{k}_{[L]}$
[B]	Target body frame	Target spacecraft	$\hat{i}_{[B]}, \hat{j}_{[B]}, \hat{k}_{[B]}$
[P]	Image frame	Sensor plane corner (2D)	$\hat{i}_{[P]}, \hat{j}_{[P]}$
[C]	Camera frame	Optical center	$\hat{i}_{[C]}, \hat{j}_{[C]}, \hat{k}_{[C]}$

Table 2
Characteristic quantities and system mass ratio in the Earth-Moon system

Length l^*	385692.50 km
Time t^*	377084.15 seconds
System mass ratio μ	0.0121505856096240

Table 1. The LVLH frame, [L], is defined with directions $\hat{i}_{[L]}, \hat{j}_{[L]}, \hat{k}_{[L]}$ such that unit direction $\hat{k}_{[L]}$ points from the target spacecraft to the central body (i.e., the Moon), $\hat{j}_{[L]}$ direction is away from the instantaneous orbital angular momentum vector, and finally, $\hat{i}_{[L]}$ completes the dextral coordinate system. Mathematically, these directions are derived as

$$\hat{k}_{[L]} = -\frac{\mathbf{r}}{||\mathbf{r}||} \tag{9}$$

$$\hat{j}_{[L]} = -\frac{\mathbf{h}}{||\mathbf{h}||} \tag{10}$$

$$\hat{i}_{[L]} = \hat{j}_{[L]} \times \hat{k}_{[L]} \tag{11}$$

where $\mathbf{r}$ represents the target position vector with respect to the central body, i.e., the Moon. Of course, the position vector $\mathbf{r}$ may be expressed in the Moon-centered rotating frame (equivalent to $\bar{r}_{[M]}$), i.e.,

$$\bar{r}_{[M]} = [x_{[M]}, y_{[M]}, z_{[M]}]^T \tag{12}$$

where superscript 'T' indicates a transpose. The instantaneous orbital angular momentum vector, $\mathbf{h}$, is the cross product of the target position vector with the target velocity vector relative to the central body ($\mathbf{v}$) at the current time, i.e., $\mathbf{h} = \mathbf{r} \times \mathbf{v}$. When expressed in the Moon-centered rotating frame [M], the target velocity is identified as $\mathbf{v} = \dot{\bar{r}}_{[M]}$. In literature, the unit directions, $\hat{i}_{[L]}, \hat{j}_{[L]}$ and $\hat{k}_{[L]}$ are sometimes denoted as V-bar, H-bar, and R-bar directions, respectively [7, 34].

The motion of the chaser relative to the target is a measure of the difference in the gravitational acceleration experienced by each target and chaser spacecraft. The acceleration for the target spacecraft, by applying Newton's laws for universal gravitation, is

$$\ddot{\mathbf{r}}_{[I]} = -\mu\frac{\mathbf{r}}{||\mathbf{r}||^3} - (1-\mu)\left(\frac{\mathbf{r} + \mathbf{r}_{em}}{||\mathbf{r} + \mathbf{r}_{em}||^3} - \frac{\mathbf{r}_{em}}{||\mathbf{r}_{em}||^3}\right) \tag{13}$$

while the acceleration due to gravitational forces experienced by the chaser is given by,

$$\ddot{\mathbf{r}}_{c[I]} = -\mu\frac{\mathbf{r}_c}{||\mathbf{r}_c||^3} - (1-\mu)\left(\frac{\mathbf{r}_c + \mathbf{r}_{em}}{||\mathbf{r}_c + \mathbf{r}_{em}||^3} - \frac{\mathbf{r}_{em}}{||\mathbf{r}_{em}||^3}\right) \tag{14}$$

where $\mathbf{r}_c$ is the chaser position vector from the central body, the Moon. The difference between the position vector of the chaser and the target provides the relative position of the chaser with respect to the target, i.e., $\bar{\rho}$, such as

$$\bar{\rho} = \mathbf{r}_c - \mathbf{r} \tag{15}$$

and the evolution of $\bar{\rho}$ offers a foundation for comprehending proximity operations. The basic kinematic equations for the velocity and the acceleration of the chaser spacecraft in the inertial frame, i.e.,

$$\dot{\mathbf{r}}_{c[I]} = \dot{\mathbf{r}}_{[I]} + \dot{\bar{\rho}}_{[I]} = \dot{\mathbf{r}}_{[I]} + \dot{\bar{\rho}}_{[L]} + \omega_{L/I} \times \bar{\rho}_{[L]} \tag{16}$$

$$\ddot{\mathbf{r}}_{c[I]} = \ddot{\mathbf{r}}_{[I]} + \ddot{\bar{\rho}}_{[L]} + 2\omega_{L/I} \times \dot{\bar{\rho}}_{[L]} + \dot{\omega}_{L/I} \times \bar{\rho}_{[L]} \\ + \omega_{L/I} \times (\omega_{L/I} \times \bar{\rho}_{[L]}) \tag{17}$$

are expressed as a function of the relative position in the LVLH frame, $\bar{\rho}_{[L]}$, as well as the angular velocity ($\omega_{L/I}$) and angular acceleration ($\dot{\omega}_{L/I}$). Moreover, the subscript L/I represents a frame transformation from the LVLH frame [L] to the inertial frame [I]. Note that, similar subscripts are defined to represent other frame transformations. Substituting Eqs. (13) and (14) into Eq. (17), the higher-order time derivatives for $\bar{\rho}_{[L]}$ are determined. The updated equation,

$$\ddot{\bar{\rho}}_{[L]} = -2\omega_{L/I} \times \dot{\bar{\rho}}_{[L]} - \dot{\omega}_{L/I} \times \bar{\rho}_{[L]} \\ - \omega_{L/I} \times (\omega_{L/I} \times \bar{\rho}_{[L]}) \\ - \mu\frac{\mathbf{r}_c}{||\mathbf{r}_c||^3} - (1-\mu)\left(\frac{\mathbf{r}_c + \mathbf{r}_{em}}{||\mathbf{r}_c + \mathbf{r}_{em}||^3} - \frac{\mathbf{r}_{em}}{||\mathbf{r}_{em}||^3}\right) \\ + \mu\frac{\mathbf{r}}{||\mathbf{r}||^3} + (1-\mu)\left(\frac{\mathbf{r} + \mathbf{r}_{em}}{||\mathbf{r} + \mathbf{r}_{em}||^3} - \frac{\mathbf{r}_{em}}{||\mathbf{r}_{em}||^3}\right) \tag{18}$$

describes the nonlinear equations for relative motion in the CR3BP [7, 35]. The angular velocity and the angular

acceleration for frame [L] relative to the inertial frame [I] is expressed as a combination of the frame rotation from LVLH to the Moon-centered rotating frame ([L] → [M]) and from the Moon-centered rotating frame to the inertial frame ([M] → [I]), such that

$$\omega_{L/I} = \omega_{L/M} + \omega_{M/I} \tag{19}$$

$$\dot{\omega}_{L/I[L]} = \dot{\omega}_{L/M} + \dot{\omega}_{M/I[M]} - \omega_{L/M} \times \omega_{M/I} \tag{20}$$

and employs the following relationships,

$$\omega_{L/M[L]} = \omega_{L/M}^x \hat{i}_{[L]} + \omega_{L/M}^y \hat{j}_{[L]} + \omega_{L/M}^z \hat{k}_{[L]} \tag{21}$$

$$\omega_{L/M}^x = 0 \tag{22}$$

$$\omega_{L/M}^y = -\frac{||\mathbf{h}||}{||\mathbf{r}||^2} \tag{23}$$

$$\omega_{L/M}^z = -\frac{||\mathbf{r}||}{||\mathbf{h}||^2} \mathbf{h} \cdot \ddot{\bar{r}}_{[M]} \tag{24}$$

that corresponds to instantaneous values for angular rotations resulting from frame transformations. The frame transformation, [L] → [M], is representative of the motion of the target body around the Moon while the frame transformation, [M] → [I] is attributed to the rotation of primary bodies, particularly the Moon around the barycenter. Using the simplifying assumptions in the CR3BP model, $\omega_{M/I} = \hat{k}_{[M]}$ is fixed; as a consequence, $\dot{\omega}_{M/I} = 0$. The quantity $\ddot{\bar{r}}_{[M]}$, such that, $\ddot{\bar{r}}_{[M]} = [\ddot{x}_{[M]}, \ddot{y}_{[M]}, \ddot{z}_{[M]}]^T$, is determined in Eqs. (4), (5) and (6). Similarly,

$$\dot{\omega}_{L/M[L]} = \dot{\omega}_{L/M}^x \hat{i}_{[L]} + \dot{\omega}_{L/M}^y \hat{j}_{[L]} + \dot{\omega}_{L/M}^z \hat{k}_{[L]} \tag{25}$$

$$\dot{\omega}_{L/M}^x = 0 \tag{26}$$

$$\dot{\omega}_{L/M}^y = -\frac{1}{||\mathbf{r}||}\left(\frac{\dot{h}}{||\mathbf{r}||} + 2\dot{r}\omega_{L/M}^y\right) \tag{27}$$

$$\dot{\omega}_{L/M}^z = \left(\frac{\dot{r}}{||\mathbf{r}||} - 2\frac{\dot{h}}{||\mathbf{h}||}\right)\omega_{L/M}^z - \frac{||\mathbf{r}||}{||\mathbf{h}||^2}\mathbf{h} \cdot \dddot{\bar{r}}_{[M]} \tag{28}$$

such that,

$$\dot{h} = -\dot{\mathbf{h}}_{[M]} \cdot \hat{j} \tag{29}$$

$$\dot{r} = \frac{1}{||\mathbf{r}||}\bar{r}_{[M]} \cdot \dot{\bar{r}}_{[M]} \tag{30}$$

including the third derivative of position, i.e., the jerk, experienced by the target spacecraft in the [M] frame,

$$\dddot{\bar{r}}_{[M]} = -2\omega_{M/I} \times \ddot{\bar{r}}_{[M]} - \omega_{M/I} \times (\omega_{M/I} \times \dot{\bar{r}}_{[M]})$$
$$- (1-\mu)\frac{\partial}{\partial \mathbf{r}}\left[\frac{\mathbf{r} + \mathbf{r}_{em}}{||\mathbf{r} + \mathbf{r}_{em}||^3}\right]\dot{\bar{r}}_{[M]} \tag{31}$$
$$- \mu\frac{\partial}{\partial \mathbf{r}}\left[\frac{\mathbf{r}}{||\mathbf{r}||^3}\right]\dot{\bar{r}}_{[M]}$$

where the following rule for differentiation applies,

$$\frac{\partial}{\partial \mathbf{q}}\left[\frac{\mathbf{q}}{||\mathbf{q}||^3}\right] = \frac{1}{||\mathbf{q}||^3}\left(\mathbf{I} - 3\frac{\mathbf{q}\mathbf{q}^T}{||\mathbf{q}||^2}\right) \tag{32}$$

for any vector $\mathbf{q}$. A simplified explicit function for jerk along each of the $x_{[M]}$, $y_{[M]}$ and $z_{[M]}$ directions are deduced in Eqs. (33), (34), and (35), such as

$$\dddot{x}_{[M]} = 2\ddot{y}_{[M]} + \dot{x}_{[M]} - \frac{\mu}{d_2^3}\left(\left(1 - 3\frac{x_{[M]}^2}{d_2^2}\right)\dot{x}_{[M]} - 3\frac{x_{[M]}y_{[M]}}{d_2^2}\dot{y}_{[M]} - 3\frac{x_{[M]}z_{[M]}}{d_2^2}\dot{z}_{[M]}\right)$$
$$- \frac{1-\mu}{d_1^3}\left(\left(1 - 3\frac{(x_{[M]}-1)^2}{d_1^2}\right)\dot{x}_{[M]} - 3\frac{(x_{[M]}-1)y_{[M]}}{d_1^2}\dot{y}_{[M]} - 3\frac{(x_{[M]}-1)z_{[M]}}{d_1^2}\dot{z}_{[M]}\right) \tag{33}$$

$$\dddot{y}_{[M]} = -2\ddot{x}_{[M]} + \dot{y}_{[M]} - \frac{\mu}{d_2^3}\left(-3\frac{x_{[M]}y_{[M]}}{d_2^2}\dot{x}_{[M]} + \left(1 - 3\frac{y_{[M]}^2}{d_2^2}\right)\dot{y}_{[M]} - 3\frac{y_{[M]}z_{[M]}}{d_2^2}\dot{z}_{[M]}\right)$$
$$- \frac{1-\mu}{d_1^3}\left(-3\frac{(x_{[M]}-1)y_{[M]}}{d_1^2}\dot{x}_{[M]} + \left(1 - 3\frac{y_{[M]}^2}{d_1^2}\right)\dot{y}_{[M]} - 3\frac{y_{[M]}z_{[M]}}{d_1^2}\dot{z}_{[M]}\right) \tag{34}$$

$$\dddot{z}_{[M]} = -\frac{\mu}{d_2^3}\left(-3\frac{x_{[M]}z_{[M]}}{d_2^2}\dot{x}_{[M]} - 3\frac{y_{[M]}z_{[M]}}{d_2^2}\dot{y}_{[M]} + \left(1 - 3\frac{z_{[M]}^2}{d_2^2}\right)\dot{z}_{[M]}\right)$$
$$- \frac{1-\mu}{d_1^3}\left(-3\frac{(x_{[M]}-1)z_{[M]}}{d_1^2}\dot{x}_{[M]} - 3\frac{y_{[M]}z_{[M]}}{d_1^2}\dot{y}_{[M]} + \left(1 - 3\frac{z_{[M]}^2}{d_1^2}\right)\dot{z}_{[M]}\right) \tag{35}$$

and evaluated numerically since analytical solutions for the set of nonlinear equations for relative motion of the chaser with respect to the target are not available.

The chaser spacecraft employs active thrusters to alter its orbit and attitude motion as mentioned previously. These thrusters exhibit additional acceleration apart from the natural dynamics. These variable acceleration values act as control parameters that are varied to achieve rendezvous. The Eq. (18) is thus modified to account for the additional relative acceleration of the chaser with control parameters u_1, u_2, u_3 as

$$
\begin{aligned}
\ddot{\bar{\rho}}_{[L]} = &- 2\Omega_{L/I[L]}\dot{\bar{\rho}}_{[L]} - (\dot{\Omega}_{L/I[L]} + \Omega^2_{L/I[L]})\bar{\rho}_{[L]} \\
&(1-\mu)\left(\frac{\mathbf{r} + \mathbf{r}_{em}}{||\mathbf{r} + \mathbf{r}_{em}||^3} - \frac{\mathbf{r} + \bar{\rho} + \mathbf{r}_{em}}{||\mathbf{r} + \bar{\rho} + \mathbf{r}_{em}||^3} \right) \\
&+ \mu\left(\frac{\mathbf{r}}{||\mathbf{r}||^3} - \frac{\mathbf{r} + \bar{\rho}}{||\mathbf{r} + \bar{\rho}||^3} \right) + [u_1, u_2, u_3]^T
\end{aligned}
\tag{36}
$$

where the following relation holds,

$$
\Omega_{L/I\,[L]} = \begin{bmatrix} 0 & -\omega^z_{L/I} & \omega^y_{L/I} \\ \omega^z_{L/I} & 0 & -\omega^x_{L/I} \\ -\omega^y_{L/I} & \omega^x_{L/I} & 0 \end{bmatrix}
\tag{37}
$$

$$
\dot{\Omega}_{L/I\,[L]} = \begin{bmatrix} 0 & -\dot{\omega}^z_{L/I} & \dot{\omega}^y_{L/I} \\ \dot{\omega}^z_{L/I} & 0 & -\dot{\omega}^x_{L/I} \\ -\dot{\omega}^y_{L/I} & \dot{\omega}^x_{L/I} & 0 \end{bmatrix}
\tag{38}
$$

$$
\omega_{L/I\,[L]} = \omega^x_{L/I}\hat{i}_{[L]} + \omega^y_{L/I}\hat{j}_{[L]} + \omega^z_{L/I}\hat{k}_{[L]}
\tag{39}
$$

$$
\dot{\omega}_{L/I\,[L]} = \dot{\omega}^x_{L/I}\hat{i}_{[L]} + \dot{\omega}^y_{L/I}\hat{j}_{[L]} + \dot{\omega}^z_{L/I}\hat{k}_{[L]}
\tag{40}
$$

and these equations are numerically integrated to identify the relative position for the chaser in the LVLH frame [L] such that

$$
\bar{\rho}_{[L]} = \rho_x\hat{i}_{[L]} + \rho_y\hat{j}_{[L]} + \rho_z\hat{k}_{[L]}
\tag{41}
$$

where ρ_x, ρ_y and ρ_z are the projections of the position vector along each of the $\hat{i}_{[L]}$, $\hat{j}_{[L]}$ and $\hat{k}_{[L]}$ directions, respectively. Such quantities in the [L] frame are also appropriate for simulating close proximity operations in a laboratory environment.

3.3. Attitude Dynamics

When the separation distance between the chaser and target spacecraft is sufficiently large, the orbital dynamics portion of the controller supersedes the attitude dynamics operations. The orientation of the chaser relative to the target is trivial at this scale. Moreover, at such a distance, optical sensors may only yield a point image of the target and the determination of relative orientation is inconsequential. However, during the final rendezvous phase such as docking, maintaining appropriate relative orientation between the chaser and target also becomes crucial. Henceforth, for convenience, the relative attitude dynamics for the chaser are

modeled with respect to the body frame of the target. Euler's equations of motion are, thus, employed to manifest the rotational dynamics of the spacecraft; the angular velocities are expressed as

$$
{}^C\dot{\omega}_1 = \frac{1}{{}^CI_1}\left(T_1 - ({}^CI_3 - {}^CI_2)\,{}^C\omega_2\,{}^C\omega_3 \right)
\tag{42}
$$

$$
{}^C\dot{\omega}_2 = \frac{1}{{}^CI_2}\left(T_2 - ({}^CI_1 - {}^CI_3)\,{}^C\omega_1\,{}^C\omega_3 \right)
\tag{43}
$$

$$
{}^C\dot{\omega}_3 = \frac{1}{{}^CI_3}\left(T_3 - ({}^CI_2 - {}^CI_1)\,{}^C\omega_1\,{}^C\omega_2 \right)
\tag{44}
$$

where ${}^C\omega \equiv \omega(Chaser \to Target)$ with a left superscript, C. The moment of inertia for the chaser along each of its three principal axes is denoted by ${}^CI_j$, with $j = 1, 2, 3$. The quantities T_1, T_2 and T_3 are components of external torques delivered by the chaser. Using the same convention the orientation is defined by quaternions ${}^C\epsilon_i \equiv \epsilon_i(Chaser \to Target)$. The orientation of the chaser is altered as desired by appropriately varying the values for T_1, T_2 and T_3. The instantaneous orientation of the chaser body relative to the target body are expressed in terms of rotation quaternions

$$
{}^C\dot{\epsilon}_1 = \frac{1}{2}\left({}^C\omega_1\,{}^C\epsilon_4 - {}^C\omega_2\,{}^C\epsilon_3 + {}^C\omega_3\,{}^C\epsilon_2 \right)
\tag{45}
$$

$$
{}^C\dot{\epsilon}_2 = \frac{1}{2}\left({}^C\omega_1\,{}^C\epsilon_3 + {}^C\omega_2\,{}^C\epsilon_4 - {}^C\omega_3\,{}^C\epsilon_1 \right)
\tag{46}
$$

$$
{}^C\dot{\epsilon}_3 = \frac{1}{2}\left(-{}^C\omega_1\,{}^C\epsilon_2 + {}^C\omega_2\,{}^C\epsilon_1 + {}^C\omega_3\,{}^C\epsilon_4 \right)
\tag{47}
$$

$$
{}^C\dot{\epsilon}_4 = \frac{1}{2}\left(-{}^C\omega_1\,{}^C\epsilon_1 - {}^C\omega_2\,{}^C\epsilon_2 - {}^C\omega_3\,{}^C\epsilon_3 \right)
\tag{48}
$$

where ϵ_1, ϵ_2 and ϵ_3 offer insight into the orientation of the axis of rotation while ϵ_4 shadows the degree of spin about the axis of rotation. Also $\epsilon_1^2 + \epsilon_2^2 + \epsilon_3^2 + \epsilon_4^2 = 1$. The dynamics of the target spacecraft are, however, assumed to be evolving under the natural gravity gradient torques exerted by the primary bodies. For simplicity, the dynamics are expressed relative to the inertial frame. Notations for the angular velocity and orientation quaternions for the target are expressed with a left superscript, T, for example, ${}^T\omega \equiv \omega(Target \to Inertial)$. The rate of change in angular velocity of the target body is given by

$$
{}^T\dot{\omega}_1 = \frac{{}^TI_3 - {}^TI_2}{{}^TI_1}\left(3\frac{1-\mu}{d_1^5}g_2g_3 + 3\frac{\mu}{d_2^5}h_2h_3 - {}^T\omega_2\,{}^T\omega_3 \right)
\tag{49}
$$

$$
{}^T\dot{\omega}_2 = \frac{{}^TI_1 - {}^TI_3}{{}^TI_2}\left(3\frac{1-\mu}{d_1^5}g_1g_3 + 3\frac{\mu}{d_2^5}h_1h_3 - {}^T\omega_1\,{}^T\omega_3 \right)
\tag{50}
$$

$$
{}^T\dot{\omega}_3 = \frac{{}^TI_2 - {}^TI_1}{{}^TI_3}\left(3\frac{1-\mu}{d_1^5}g_1g_2 + 3\frac{\mu}{d_2^5}h_1h_2 - {}^T\omega_1\,{}^T\omega_2 \right)
\tag{51}
$$

where the terms including $(1-\mu)$ quantify the effects of the gravity torque due to body P1, i.e., the Earth; while terms including μ are associated with the gravity gradient torque exerted by body P2, i.e., the Moon [4, 10]. The quantities g_j and

$$
\begin{bmatrix} g_1 \\ g_2 \\ g_3 \end{bmatrix} = \begin{bmatrix} {}^T\dot{\epsilon}_1{}^2 - {}^T\dot{\epsilon}_2{}^2 - {}^T\dot{\epsilon}_3{}^2 + {}^T\dot{\epsilon}_4{}^2 & 2({}^T\dot{\epsilon}_1{}^T\dot{\epsilon}_2 + {}^T\dot{\epsilon}_3{}^T\dot{\epsilon}_4) & 2({}^T\dot{\epsilon}_1{}^T\dot{\epsilon}_3 - {}^T\dot{\epsilon}_2{}^T\dot{\epsilon}_4) \\ 2({}^T\dot{\epsilon}_1{}^T\dot{\epsilon}_2 - {}^T\dot{\epsilon}_3{}^T\dot{\epsilon}_4) & -{}^T\dot{\epsilon}_1{}^2 + {}^T\dot{\epsilon}_2{}^2 - {}^T\dot{\epsilon}_3{}^2 + {}^T\dot{\epsilon}_4{}^2 & 2({}^T\dot{\epsilon}_2{}^T\dot{\epsilon}_3 + {}^T\dot{\epsilon}_1{}^T\dot{\epsilon}_4) \\ 2({}^T\dot{\epsilon}_1{}^T\dot{\epsilon}_3 + {}^T\dot{\epsilon}_2{}^T\dot{\epsilon}_4) & 2({}^T\dot{\epsilon}_2{}^T\dot{\epsilon}_3 - {}^T\dot{\epsilon}_1{}^T\dot{\epsilon}_4) & -{}^T\dot{\epsilon}_1{}^2 - {}^T\dot{\epsilon}_2{}^2 + {}^T\dot{\epsilon}_3{}^2 + {}^T\dot{\epsilon}_4{}^2 \end{bmatrix}
$$
$$
\begin{bmatrix} cos(\dot{\theta}\tau) & -sin(\dot{\theta}\tau) & 0 \\ sin(\dot{\theta}\tau) & cos(\dot{\theta}\tau) & 0 \\ 0 & 0 & 1 \end{bmatrix} \begin{bmatrix} 1 - x_{[M]} \\ -y_{[M]} \\ z_{[M]} \end{bmatrix} \tag{52}
$$

$$
\begin{bmatrix} h_1 \\ h_2 \\ h_3 \end{bmatrix} = \begin{bmatrix} {}^T\dot{\epsilon}_1{}^2 - {}^T\dot{\epsilon}_2{}^2 - {}^T\dot{\epsilon}_3{}^2 + {}^T\dot{\epsilon}_4{}^2 & 2({}^T\dot{\epsilon}_1{}^T\dot{\epsilon}_2 + {}^T\dot{\epsilon}_3{}^T\dot{\epsilon}_4) & 2({}^T\dot{\epsilon}_1{}^T\dot{\epsilon}_3 - {}^T\dot{\epsilon}_2{}^T\dot{\epsilon}_4) \\ 2({}^T\dot{\epsilon}_1{}^T\dot{\epsilon}_2 - {}^T\dot{\epsilon}_3{}^T\dot{\epsilon}_4) & -{}^T\dot{\epsilon}_1{}^2 + {}^T\dot{\epsilon}_2{}^2 - {}^T\dot{\epsilon}_3{}^2 + \dot{\epsilon}_4{}^2 & 2({}^T\dot{\epsilon}_2{}^T\dot{\epsilon}_3 + {}^T\dot{\epsilon}_1{}^T\dot{\epsilon}_4) \\ 2({}^T\dot{\epsilon}_1{}^T\dot{\epsilon}_3 + {}^T\dot{\epsilon}_2{}^T\dot{\epsilon}_4) & 2({}^T\dot{\epsilon}_2{}^T\dot{\epsilon}_3 - {}^T\dot{\epsilon}_1{}^T\dot{\epsilon}_4) & -{}^T\dot{\epsilon}_1{}^2 - {}^T\dot{\epsilon}_2{}^2 + {}^T\dot{\epsilon}_3{}^2 + {}^T\dot{\epsilon}_4{}^2 \end{bmatrix}
$$
$$
\begin{bmatrix} cos(\dot{\theta}\tau) & -sin(\dot{\theta}\tau) & 0 \\ sin(\dot{\theta}\tau) & cos(\dot{\theta}\tau) & 0 \\ 0 & 0 & 1 \end{bmatrix} \begin{bmatrix} -x_{[M]} \\ -y_{[M]} \\ z_{[M]} \end{bmatrix} \tag{53}
$$

where $\dot{\theta}\tau$ symbolizes the angle between the frames [S] and [I] in the CR3BP. The nondimensional value for $\dot{\theta}$ in CR3BP is 1; τ is the nondimensional time. Consistently, the orientation of the target spacecraft is governed by the following equations for the quaternions

$$
{}^T\dot{\epsilon}_1 = \frac{1}{2}\left({}^T\omega_1{}^T\epsilon_4 - {}^T\omega_2{}^T\epsilon_3 + {}^T\omega_3{}^T\epsilon_2\right) \tag{54}
$$

$$
{}^T\dot{\epsilon}_2 = \frac{1}{2}\left({}^T\omega_1{}^T\epsilon_3 + {}^T\omega_2{}^T\epsilon_4 - {}^T\omega_3{}^T\epsilon_1\right) \tag{55}
$$

$$
{}^T\dot{\epsilon}_3 = \frac{1}{2}\left(-{}^T\omega_1{}^T\epsilon_2 + {}^T\omega_2{}^T\epsilon_1 + {}^T\omega_3{}^T\epsilon_4\right) \tag{56}
$$

$$
{}^T\dot{\epsilon}_4 = \frac{1}{2}\left(-{}^T\omega_1{}^T\epsilon_1 - {}^T\omega_2{}^T\epsilon_2 - {}^T\omega_3{}^T\epsilon_3\right) \tag{57}
$$

that offer the rate of change of the orientation of the target body axis relative to the inertial frame.

Mathematical solutions for the chaser trajectory may pass through the body of the target. The chaser and target spacecraft are rigid bodies, however, and such a rendezvous path is not feasible. Thus, during the rendezvous, the chaser spacecraft is deliberately constrained to remain at a fixed distance from the center of the target spacecraft without colliding. For convenience, such a location is labeled as "approach site," and is stationary in the body-fixed frame of the target, [B]. The chaser must eventually progress towards the "approach site" during rendezvous. The coordinates of the approach site, however, are neither static in the inertial frame [I], the Moon-centered rotating frame [M] nor the LVLH coordinate frame [L] due to continuous frame transformations. The target spacecraft may appear as tumbling in a particular frame of interest; as a consequence, the approach site is rather an instantaneous 3-dimensional location, as illustrated in Figure 3. In this investigation, for convenience, the approach site is assumed as the eventual location of the geometric center of the chaser spacecraft during rendezvous.

Consider the coordinates of the approach site as

$$
\bar{\varrho}_{[B]} = b_1\hat{i}_{[B]} + b_2\hat{j}_{[B]} + b_3\hat{k}_{[B]}
$$

measured in the target body frame and along its principal axes of inertia. Note that b_1, b_2 and b_3 are fixed parameters selected as desired. The LVLH frame is conveniently the working frame of view and offers direct insight into the spacecraft's approach during the rendezvous process. The "approach site" in the LVLH frame is deduced as

$$
\bar{\varrho}_{[L]} = \begin{pmatrix} \varrho_x \\ \varrho_y \\ \varrho_z \end{pmatrix} = {}^{[L]}\mathbb{C}^{[B]} \quad \bar{\varrho}_{[B]} = {}^{[L]}\mathbb{C}^{[B]} \begin{pmatrix} b_1 \\ b_2 \\ b_3 \end{pmatrix}
$$

where ${}^{[L]}\mathbb{C}^{[B]} = \{\mathbb{C} : [B] \rightarrow [L]\}$ is the transformation matrix from the target body frame [B] to the LVLH frame [L]. The matrix ${}^{[L]}\mathbb{C}^{[B]}$,

$$
{}^{[L]}\mathbb{C}^{[B]} = {}^{[L]}\mathbb{C}^{[M]} \ {}^{[M]}\mathbb{C}^{[I]} \ {}^{[I]}\mathbb{C}^{[B]} \tag{58}
$$

is a by-product of a sequence of frame rotations, i.e., [B] → [I], [I] → [M] and finally [M] → [L]. The transformation matrix or the Direction Cosine Matrix (DCM), ${}^{[I]}\mathbb{C}^{[B]}$, is evaluated from the orientation quaternions, ${}^T\epsilon$. From the definition in the CR3BP model, $\omega_{M/I} = \hat{k}_{[M]}$ and remains fixed; as a consequence, the [M] frame rotates about the inertial frame [I] at a consistent rate proportional to the nondimensional time τ. Thus, the calculation of the transformation matrix ${}^{[M]}\mathbb{C}^{[I]}$ is enabled. Finally, the correlations in Eq. (11) facilitate determination of matrix ${}^{[L]}\mathbb{C}^{[M]}$.

Mathematically, the progression of the chaser spacecraft towards the approach site during the rendezvous operations is denoted by, $\bar{\rho}_{[L]} \rightarrow \bar{\varrho}_{[L]}$, i.e., $\rho_x \rightarrow \varrho_x$, $\rho_x \rightarrow \varrho_y$ and $\rho_z \rightarrow \varrho_z$. A chaser spacecraft may not necessarily dock along any particular principal axis of the target. Incorporating the approach site while modeling the rendezvous process facilitates defining complex docking scenarios.

h_j, with $j = 1, 2, 3$, represent the projections of the position vectors to P1 and P2 on the target body frame, respectively [4, 5]. These quantities are evaluated in Eqs. (52) and (53), such as
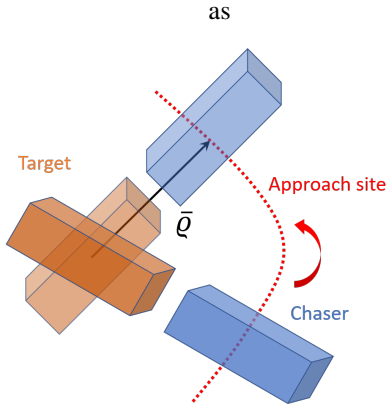

Figure 3: Approach site, $\bar{\varrho}$, for the chaser as a 3D location relative to the center of the target [8].

4. Guidance: Optimal Path Planning

The dynamics for the spacecraft trajectory and attitude dynamics are complex and nonlinear. To facilitate the determination of an optimal guidance path suitable for proximity operations, a nonlinear control algorithm, CasADi, [36] is introduced with an Interior Point Optimization (IPOPT) scheme. A cost functional, J, such that

$$J = \int_0^\tau (\bar{\rho}_{[L]} - \bar{\varrho}_{[L]})^T \mathbf{Q}_1 (\bar{\rho}_{[L]} - \bar{\varrho}_{[L]}) + {}^C\bar{\omega}^T \mathbf{Q}_2 {}^C\bar{\omega}$$
$$+ {}^C\bar{\epsilon}^T \mathbf{Q}_3 {}^C\bar{\epsilon} + \mathbf{u}^T \mathbf{R} \mathbf{u} \quad dt \quad (59)$$

is minimized during the optimization process. Here weighting matrix $\mathbf{Q}_1$ penalizes any offset in position states from the approach site, i.e., $\bar{\rho}_{[L]} - \bar{\varrho}_{[L]}$. The relative angular velocity of the chaser with respect to the target is compensated by matrix $\mathbf{Q}_2$ whereas the relative change in orientation between the two spacecraft is penalized by matrix $\mathbf{Q}_3$. Finally, the control inputs $\mathbf{u}$ are weighted with matrix $\mathbf{R}$. The control input vector $\mathbf{u}_k$ is defined as,

$$\mathbf{u}_k = [u_1, u_2, u_3, T_1, T_2, T_3]^T$$

where u_1, u_2 and u_3 represent translational acceleration along each of the x, y and z directions, respectively; T_1, T_2 and T_3 (also referred as u_4, u_5 and u_6) are the control torques that the chaser spacecraft may deliver. Alternate rendezvous paths are obtained by varying each of the penalty matrices within the cost functional J. Further, an additional collision avoidance constraint is introduced as

$$||\bar{\rho}|| \geq r_{collision}$$

to maintain the position of the chaser spacecraft outside a spherical volume centered at the target spacecraft with a radius $r_{collision}$. The quantity $r_{collision}$ is user-defined, typically larger than the dimensions of the spacecraft along

appropriate directions. The optimal control process yields states (both trajectory and attitude) that serve as the baseline or the predicted reference path for rendezvous operations. Such a guidance path is ideal and void of any fluctuations or uncertainties. An actual path, however, incorporates inherent errors. Consequently, the state estimation and linear control algorithms are engaged synchronously during the entire proximity operations.

5. Vision Based Navigation

Relative state estimation in proximity operations supported by perceptual observations is crucial for robust autonomous navigation systems. These perceptual observations may be available from one or more sensors like cameras, Lidars and Radars. With the advent of advanced vision algorithms and increasing computational availability, visible spectrum cameras have become a favorable choice for perception due to their small form factors, low power consumption and cost-effectiveness. For the problem of target localization, as addressed in this work, a range of different approaches may be employed. For instance, if the target does not have uniquely identifiable fiducial markers, feature-based, template-based or neural network based pose estimation may be used [37, 38]. In this investigation, however, a simplified perception using pre-defined passive fiducial markers is considered for engaging the rendezvous scenario in a closed-loop manner. The usage of such markers is common in cooperative proximity operations. Owing to their superior balance of performance, speed, and detection reliability, an array of fiducial ArUco [39, 40] markers are used on the target spacecraft mockup. Unique detection of each ArUco marker is facilitated by its encoding dictionary[41], which provides a unique combination of n_exn_e array of bits that take a binary value. ArUco markers provide reasonably precise localization of the four corners that enclose them. Identification and localization are accomplished within the ArUco detection algorithm by first applying an adaptive threshold to the image and polygonalizing the filtered contours. Subsequently, the quadrilaterals are filtered and binary bit codes inside the quadrilaterals are parsed for identification. Given valid identification of a marker, marker identifier or ID in the marker dictionary and then the ordered pair of corner coordinates are obtained. Once the locations of marker corners are obtained, the pose of the known body frame relative to the camera is estimated using the Perspective-n-Points formulation.

Given knowledge of the target's 3D wireframe model, the intrinsic parameters of the observing camera (found by calibration), and the 2D location of the feature in the image plane, the perspective geometry and projection of the points between 3D and 2D spaces is described by the PnP formulation, and demonstrated in Fig. 4. Consider

$$r_{[B]} = [x_{j[B]}, \; y_{j[B]}, \; z_{j[B]}]^T$$

with $j = 1, 2, 3...n$ to be n points of interest on a known 3D model in the body frame, [B], and $p_j = [u_j, v_j]^T$, be

n corresponding image points in the 2D image frame, [P]. The PnP problem concerns the projection of object or body points to image points, subject to the camera's intrinsic and extrinsic parameters. The extrinsic parameters specify a 3D-3D transform to project points in the body frame to the camera frame. The intrinsic parameters specify the 3D-2D transformation that projects the points in the camera frame to the image plane. For an arbitrary 3D point $r_{[B]}$ in an object's body frame, the corresponding projection, $r_{[C]}$, in the camera frame and the 2D projection p in the image frame are then expressed as

$$r_{[C]} = {}^{[C]}\mathbb{C}^{[B]} \, r_{[B]} + t_{[C]} \tag{60}$$

$$p = \left[\frac{x_{[C]}}{y_{[C]}} f_x + C_x \, , \, \frac{y_{[C]}}{z_{[C]}} f_y + C_y \right] \tag{61}$$

where intrinsic parameters, f_x and f_y are focal lengths in the respective principle directions of the image frame, while C_x and C_y are locations of the principle points of the projected image. The rotation matrix ${}^{[C]}\mathbb{C}^{[B]}$ and the translation vector $t_{[C]}$ specify the extrinsic parameters. To further condition the generic problem, it is assumed that the unit vector $\hat{k}_{[C]}$ direction is along the bore-sight of the camera, and the unit vectors $\hat{i}_{[C]}$ and $\hat{j}_{[C]}$ are aligned with the image frame axes $\hat{i}_{[P]}$ and $\hat{j}_{[P]}$. In that case, the Eqs. (60) & (61) are transformed using homogeneous coordinates and expanded as

$$\begin{bmatrix} w_j u_j \\ w_j v_j \\ w_j \end{bmatrix} = \begin{bmatrix} \mathcal{K} \end{bmatrix} \begin{bmatrix} \mathcal{P} \end{bmatrix} \begin{bmatrix} x_{j[B]} \\ y_{j[B]} \\ z_{j[B]} \\ 1 \end{bmatrix} \tag{62}$$

where, $\mathcal{K}$ is 3x3 camera intrinsic matrix, $\mathcal{P}$ is the 4x3 pose matrix for extrinsic transformation, and w is the scale factor for the image point. Assuming zero distortion and square sensor pixels, Eq. (62) is expanded to

$$\begin{bmatrix} w_j u_j \\ w_j v_j \\ w_j \end{bmatrix} = \begin{bmatrix} f_x & 0 & C_x \\ 0 & f_y & C_y \\ 0 & 0 & 1 \end{bmatrix} \begin{bmatrix} {}^{[C]}\mathbb{C}^{[B]} & | & t_{[C]} \end{bmatrix} \begin{bmatrix} x_{j[B]} \\ y_{j[B]} \\ z_{j[B]} \\ 1 \end{bmatrix} \tag{63}$$

and has 6 unknowns in $\mathcal{P}$ that include three independent parameters for relative attitude and three for relative position. These unknown parameters are estimated using analytical methods exploiting geometry or iterative methods optimizing a reprojection objective.

Generally, $n = 6$ points in a non-coplanar configuration are ideal for unambiguous estimation of the relative pose, as a lower number of points results in multiple ambiguous pose solutions. Since 2D fiducial markers like ArUco provide four co-planar corners, perspective ambiguity is inevitable [42]. Such ambiguities result from multiple local minima from relative poses that minimize the reprojection cost to similar magnitudes. To overcome the ambiguity issues, along with any practical shortcomings of precision along the range, partial occlusions, and specular blinding, an array of seven ArUco markers are used with different
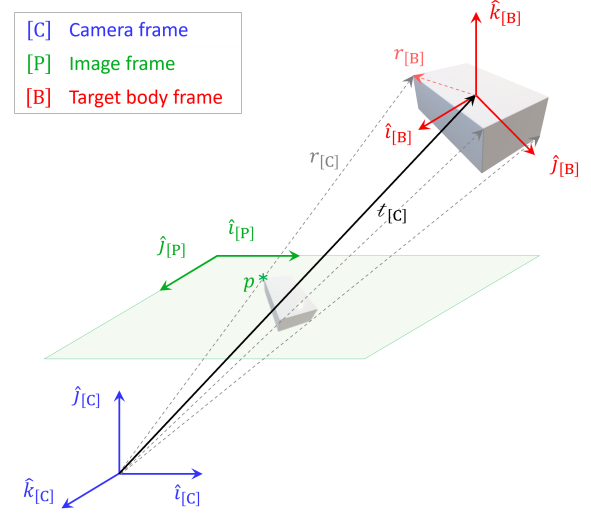

Figure 4: Frame descriptions for PnP problem.

sizes such that locations of corners minimize the presence of axes of symmetry under different combinations of detection. The marker dictionary uses 4x4 ($n_e = 4$) encoding bits and has a minimum hamming distance between marker pairs of 4. It reduces misdetections while providing high-bit resolution in the threshold image along the range. Once marker corners are localized, an EPnP solver [43] is used to solve for relative pose using the 3D-2D correspondences in the known wireframe model in the body frame. While the EPnP solver provides reliable pose estimates, false positive detection of marker corners may result in degraded pose estimates. To mitigate this issue, a Random Sample Consensus (RANSAC) [44] is used with EPnP to reject corner outliers. Figure 5 illustrates the detection of seven ArUco markers and the resulting marker plane pose on the mock-up of the target spacecraft.
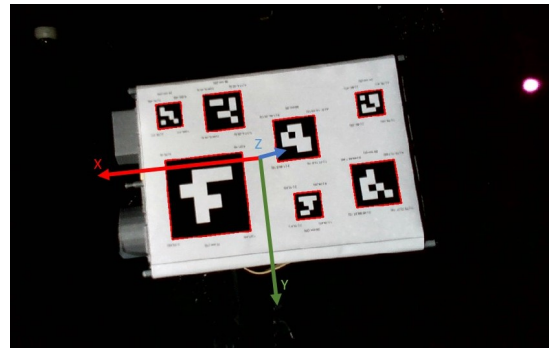

Figure 5: ArUco markers on target CubeSat mock-up identified for pose estimation.

6. Estimation and Control

6.1. State Estimation

When the separation distance between the spacecraft is relatively small, optical sensors, typically in the form of visible light or infrared cameras that are attached to the chaser spacecraft, are capable of determining the position and orientation vectors (also denoted as the "pose") of a target spacecraft, or perhaps any other target object including space debris. Modern sensors can capture pose data at a frequency of as much as 20 Hz; pose observations are, thus, acquired at discrete time intervals. Rudimentary observations may incur large fluctuations and inherent uncertainties. Implementing control maneuvers in response to every individual observation is redundant and potentially draws large control costs. Individual observations are, therefore, filtered to determine state estimates with reasonable precision. A measurement matrix consisting of partial derivatives of observed quantities (pose, in this case) with respect to the state variables, is the basis of a filtering process. The most common filters for trajectory and attitude estimation are Batch Least Squares and a sequential Kalman filter. State estimates and covariance matrices are updated in succession allowing prior observations to be discarded in a sequential Kalman filter. A sequential Kalman filter, therefore, offers an advantage over a batch least squares filter in terms of computational memory allocation [9, 45]; and is, subsequently, selected for this analysis.

6.1.1. System Dynamics

Appropriate prediction of spacecraft states at a certain time is key to designing an estimator and a controller. Consider the configuration of the system described by the state vector $\mathbf{x}$, i.e.,

$$\mathbf{x} = [x_{[M]}, y_{[M]}, z_{[M]}, \dot{x}_{[M]}, \dot{y}_{[M]}, \dot{z}_{[M]},$$
$$\rho_x, \rho_y, \rho_z, \dot{\rho}_x, \dot{\rho}_y, \dot{\rho}_z,$$
$${}^C\omega_1, {}^C\omega_2, {}^C\omega_3, {}^C\epsilon_1, {}^C\epsilon_2, {}^C\epsilon_3, {}^C\epsilon_4,$$
$${}^T\omega_1, {}^T\omega_2, {}^T\omega_3, {}^T\epsilon_1, {}^T\epsilon_2, {}^T\epsilon_3, {}^T\epsilon_4, x_\varrho, y_\varrho, z_\varrho]^{\mathrm{T}}$$

that captures the motion of the target spacecraft in the Moon-centered rotating frame, the position, velocity and orientation of the chaser spacecraft relative to the target, the orientation of the target in the inertial frame, and the instantaneous locus of the approach site. In principle, the orientation of the target spacecraft as well as the coordinates of the approach site evolve independently (or decoupled) from the motion of the chaser spacecraft. As a consequence, pose observations or corresponding maneuvers do not affect the motion of the target spacecraft.

Observed data are processed by the Kalman filter and provide updates to the covariance and estimates of the states within the stochastic system. Computational speed is key when applied to a system that runs in real-time. Correspondingly, the Kalman filter is developed upon a linearized system of state equations along the predetermined baseline optimal path for the spacecraft motion. The equations are as

formulated as

$$\delta\mathbf{x}_{j+1} = \mathbf{A}_j \delta\mathbf{x}_j + \mathbf{B}_j \Delta\mathbf{v}_j + \mathbf{w}_j \tag{64}$$
$$\delta\mathbf{y}_{j+1} = \mathbf{H}_j \delta\mathbf{x}_j + \mathbf{e}_j \tag{65}$$

where $\mathbf{A}_j$ and $\mathbf{B}_j$ are system matrices, $\mathbf{H}_j = \frac{\partial \mathbf{y}}{\partial \mathbf{x}}$ is the measurement matrix, whereas $\mathbf{w}_j$ and $\mathbf{e}_j$ are stochastic white noise with covariance $E[\mathbf{w}_j\mathbf{w}_j^{\mathrm{T}}] = \mathbb{Q}$ and $E[\mathbf{e}_j\mathbf{e}_j^{\mathrm{T}}] = \mathbb{R}$, respectively. The frequency of the control inputs differs from the sampling frequency resulting in $\Delta\mathbf{v}_j = 0$ at certain time instants t_j.

6.1.2. Filtering

The Kalman filter is developed based upon an inherent assumption that the noises, $\mathbf{w}_j$ and $\mathbf{e}_j$, are Gaussian. These assumptions are reasonable and deliver rational results for a number of space applications [9]. The sequential Kalman filter minimizes the mean square error of the estimated states from the reference. The state estimates and the covariance are derived as

$$\delta\hat{\mathbf{x}}_{j|j} = \delta\hat{\mathbf{x}}_{j|j-1} + \mathbb{K}_j \delta\mathbf{y}_j \tag{66}$$
$$\mathbf{\Sigma}_{j|j} = \mathbf{\Sigma}_{j|j-1} - \mathbb{K}'_j \mathbf{H}_j \mathbf{\Sigma}_{j|j-1} \tag{67}$$
$$\mathbb{K}'_j = \mathbf{\Sigma}_{j,j-1} \mathbf{H}_j^T (\mathbf{H}_j \mathbf{\Sigma}_{j|j-1} \mathbf{H}_j^T + \mathbb{R})^{-1} \tag{68}$$
$$\mathbf{\Sigma}_{j+1|j} = \mathbf{A}_j \mathbf{\Sigma}_{j|j} \mathbf{A}_j^T + \mathbb{Q}_j \tag{69}$$

where $\delta\hat{\mathbf{x}}_{j|j-1}$ is the predicted state estimate once $j-1$ observations are available prior to the j-th observation, and $\delta\hat{\mathbf{x}}_{j|j}$ is the new estimate once the measurement at j-th observation is also included. The Kalman gain, $\mathbb{K}$, is a by-product of the system matrices, measurement covariance and state covariance. The quantity,

$$\mathbf{\Sigma}_{j|j-1} = E[(\delta\mathbf{x}_j - \delta\hat{\mathbf{x}}_{j|j-1})(\delta\mathbf{x}_j - \delta\hat{\mathbf{x}}_{j|j-1})^{\mathrm{T}}] \tag{70}$$

is the *a-priori* state covariance at the j-th interval once $j-1$ observations are filtered. Then, the covariance matrix

$$\mathbf{\Sigma}_{j|j} = E[(\delta\mathbf{x}_j - \delta\hat{\mathbf{x}}_{j|j})(\delta\mathbf{x}_j - \delta\hat{\mathbf{x}}_{j|j})^{\mathrm{T}}] \tag{71}$$

is the *a-posteriori* covariance after the j-th observation is also incorporated. Initially, prior to the availability of any observed data, the value of *a-priori* covariance $\mathbf{\Sigma}_{j|j-1}$ is set high. The covariance matrices and state estimates are continuously updated with the availability of additional observations. The control maneuvers are delivered at a smaller frequency than the pose tracking data, allowing sufficient observations to be captured to produce reliable state estimates.

6.2. Linear Controller

A nonlinear controller is well suited for sophisticated problems that include a set of nonlinear equations of motion and multiple complex constraints. Subsequently, the nonlinear controller is the primary choice for identifying the baseline rendezvous path. The benefits offered by the nonlinear controller are sometimes offset by the excess computational time to determine an optimal solution. Rapid computation

of control maneuvers, therefore, is challenging. For successful practical application, the nonlinear controller must be computationally compatible and operate in sync with any onboard software; perhaps, compute the maneuvers at a pace faster than the actual flight time. A nonlinear controller is, therefore, not employed for the routine maneuver delivery process but rather to yield a baseline flight path adequate for rendezvous, typical of any flagship mission.

A linear controller allows significantly quicker calculations appropriate for delivering maneuvers that compensate for any deviations detected from the predetermined baseline path and is engaged in tandem with the nonlinear guidance algorithm. A linear controller is appropriate for systems that obey the superposition principle [46]. The dynamical flow in the neighborhood of the baseline path is linearized and modeled using state-space representation, analogous to that adopted for the Kalman filter. Accordingly, the state transition matrices (or system matrices) are computed for each discrete control segment along the predetermined nonlinear baseline path.

A two-layered guidance and control approach is implemented in this investigation to exploit the advantages offered by both the nonlinear and linear controllers. The approach is detailed as follows

- First and foremost, the nonlinear controller using an IPOPT scheme generates an ideal baseline rendezvous path for guidance, with a sequence of optimal control maneuvers, $\mathbf{u}_k^*$. If perturbations or modeling errors are absent, the baseline rendezvous path guides the chaser spacecraft toward the target. However, in practice, perturbations are inherent and inevitable. Any deviations from this baseline path must also be compensated.

- As the chaser progresses toward the target, the navigation apparatus offer relative pose observations that are continuously recorded and serve as feedback to the chaser's motion. The Kalman filter offers the state estimate from these pose observations. The linear controller determines subsequent maneuvers to compensate for the measured deviations from the baseline path.

Figure 6 offers a schematic of the two-layered guidance and control regime adopted in this investigation. The nonlinear controller yields the baseline path indicated in red while the green curve indicates the true path. Quantities marked with an asterisk, $*$, mark the state and controls along the baseline guidance path whereas the state and controls along the true path are denoted without the asterisk. At initial time, t_0, the control output is $\mathbf{u}_0$; also $\mathbf{u}_0 = \mathbf{u}_0^*$. Subsequently, the linear controller produces corrective maneuvers, $\delta\mathbf{u}_k$, at time t_k. The total control maneuver ($\mathbf{u}_k$) delivered to the chaser spacecraft along its true path is the total sum of the control outputs from the nonlinear ($\mathbf{u}_k^*$) and the linear controller ($\delta\mathbf{u}_k$), i.e., $\mathbf{u}_k = \mathbf{u}_k^* + \delta\mathbf{u}_k$. For convenience, the control outputs of the nonlinear and linear controllers are engaged at the same frequency. Figure 7 offers a summary of the rendezvous process; one that exploits a two-layered

approach with a blended linear and nonlinear controller, with state feedback and closed-loop hardware simulations.
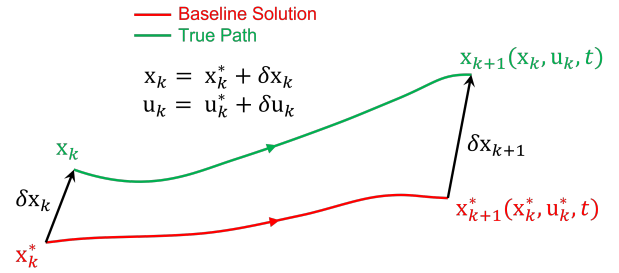
Figure 6: The baseline/reference solution is computed with nonlinear control while the spacecraft's true path incorporates maneuvers from the linear controller. The spacecraft's true path incorporates deviations from the reference [8].
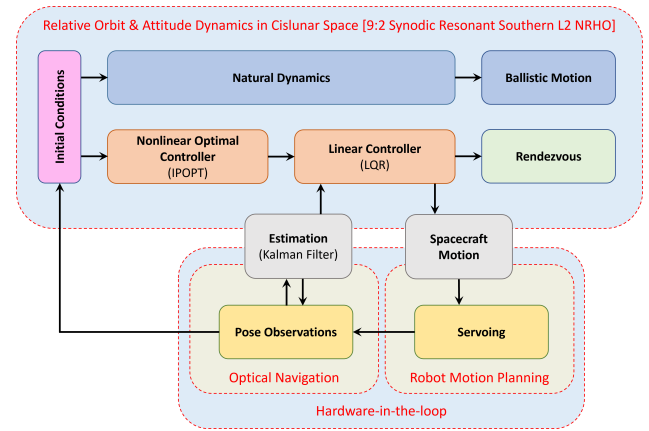
Figure 7: Overview of the proximity operations [16].

6.2.1. System Dynamics

Limitations in navigational apparatus and modeling errors induce perturbations to the spacecraft flight path, both in orbit and attitude, therefore, appropriate control strategies are adopted to maintain the spacecraft in close proximity to the reference path. Quick control response to compensate for any deviations measured from the baseline path, i.e., the quantity $\delta\mathbf{x}_k$ is adopted using the linear controller. The state errors are typically small, and hence, linearized dynamics in the neighborhood of the reference path is a good approximation to predict the necessary control output. The linear variational equations of motion are thus computed as

$$\delta\mathbf{x}_{k+1} = \mathbf{A}_k\delta\mathbf{x}_k + \mathbf{B}_k\delta\mathbf{u}_k \tag{72}$$

where $\mathbf{A}_k$ is the 29×29 state transition matrix, and $\mathbf{B}_k$ is a 29×6 matrix with partials of the state vector at the final time, $\mathbf{x}_{k+1}$, to a control input $\delta\mathbf{u}_k$, evaluated along the baseline path. The motion of the target spacecraft and the approach site are decoupled and independent from the motion of the chaser spacecraft; a number of partials within the matrix $\mathbf{A}_k$ are therefore zeros, resulting in a sparse

matrix. Further, by definition, only the chaser spacecraft possesses control capabilities while the target only evolves under natural dynamics. Consequently, the control inputs only alter the flight path of the chaser and do not influence the motion of the target body or the location of the approach site. A number of partials within matrix $\mathbf{B}_k$ are subsequently zeros. The matrices $\mathbf{A}_k$ and $\mathbf{B}_k$ are numerically computed using a central differencing technique.

6.2.2. Linear Quadratic Regulator (LQR)

Given the linearized dynamical flow near a desired path, a linear quadratic regular offers a cost-optimal control. A discrete LQR controller is designed to update control maneuvers at regular intervals. As the feedback from the Kalman filter is received, the deviation from the desired reference is known. A cost functional, $\tilde{J}$, is defined as

$$\tilde{J} = \delta\mathbf{x}_N^\mathsf{T}\tilde{\mathbf{P}}_N\delta\mathbf{x}_N + \sum_{k=0}^{N-1}\delta\mathbf{x}_k^\mathsf{T}\tilde{\mathbf{Q}}_k\delta\mathbf{x}_k + \delta\mathbf{u}_k^\mathsf{T}\tilde{\mathbf{R}}_k\delta\mathbf{u}_k \quad (73)$$

and minimized in the process. Any deviations from the baseline states are penalized. Weights are also introduced on the size of the control outputs. The solution to minimizing the cost functional is given by [47, 48],

$$\delta\mathbf{u}_k = -\tilde{\mathbf{K}}_k\delta\mathbf{x}_k \quad (74)$$

where $\tilde{\mathbf{K}}_k$ is the set of time-varying gain matrices that satisfy

$$\tilde{\mathbf{K}}_k = (\tilde{\mathbf{R}}_k + \mathbf{B}_k^\mathsf{T}\tilde{\mathbf{P}}_{k+1}\mathbf{B}_k)^{-1}\mathbf{B}_k^\mathsf{T}\tilde{\mathbf{P}}_{k+1}\mathbf{A}_k \quad (75)$$

and $\tilde{\mathbf{P}}_k$ is determined by solving the discrete algebraic Riccati equation,

$$\tilde{\mathbf{P}}_k = \tilde{\mathbf{Q}}_k + \mathbf{A}_k^\mathsf{T}\tilde{\mathbf{P}}_{k+1}\mathbf{A}_k - \mathbf{A}_k^\mathsf{T}\tilde{\mathbf{P}}_{k+1}\mathbf{B}_k\tilde{\mathbf{K}}_k \quad (76)$$

for $k = 0, \dots, N-1$. The quantities $\tilde{\mathbf{Q}}_k$ and $\tilde{\mathbf{R}}_k$ are positive definite weighting matrices or penalty matrices. The value of N is the total number of discrete control intervals selected for the rendezvous operations.

Pose observations are retrieved and processed through a Kalman filter at a significantly high frequency to overcome large fluctuations and, subsequently, obtain reliable state estimates. Controllers, however, operate at a lower frequency than the estimator. Moreover, it is desired to span two successive control maneuvers sufficiently apart to achieve a reasonable estimate of the spacecraft's position, velocity and orientation states. A schematic representation of the overall process from the procurement of pose observations to state estimation and, finally, delivering control outputs are established in a timeline and presented in Fig. 8. The schematic emphasizes the following:

- Note that in the absence of any control maneuvers the chaser spacecraft evolves under the underlying natural dynamics and the resulting ballistic motion, given by a solid blue curve, may not advance toward the target.

- An appropriate guidance trajectory analogous to the red curve serves as the predetermined baseline for the rendezvous operations; this baseline is determined by the nonlinear optimal control algorithm.

- Prominent red dots lie along the baseline path and correspond to discrete time intervals where the optimal control maneuvers are updated.

- Pose observations recorded by the camera on the chaser spacecraft are symbolized by magenta dots and occur at a high frequency.

- The observed navigation data is processed through the Kalman filter to yield an estimate, reflected as the gray dotted curve.

- The actual spacecraft trajectory is labeled as the true path and is illustrated by the green curve in Fig. 8. Deviations due to uncertainties in the state measurements and unmodeled errors are inherited into the true path; consequently, the true path does not precisely overlap the red curve but rather exists in the neighborhood of the baseline.
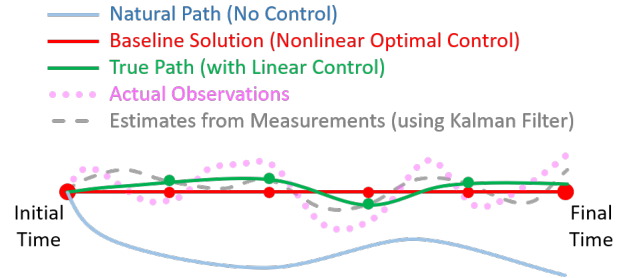

Figure 8: Schematic timeline of the natural ballistic path, optimal path for rendezvous, and true path. Red and green dots correspond to discrete time intervals of control outputs, while magenta dots correspond to pose observations recorded by the optical navigation sensors.

7. Robot Motion Planning

7.1. Experimental Setup

The ZeroG Lab at the University of Luxembourg is a robotic test facility for real-time simulation of on-orbit servicing missions. As demonstrated in Fig. 9, the facility is a 5m x 3m area. The facility has four main components to emulate on-orbit scenarios: a Sun emulator to recreate the challenging space lighting conditions, a 240 Hz advanced Motion Capture System (MCS) to provide ground truth data, and two UR10e robotic manipulators. Each robotic manipulator has six degrees-of-freedom and is mounted on a rail to provide an additional range of motion suitable for simulating spacecraft motion in on-orbit scenarios. The UR10e robots, the MCS as well as other external devices communicate and are controlled using the Robot Operating System (ROS). External commands to control these robotic manipulators are also directed over the ROS network. A mock-up of the

target spacecraft is mounted on the ceiling arm's flange. Likewise, the mock-up simulating the chaser spacecraft, in the form of an optical camera, is mounted on the wall robotic arm. A schematic representation of the laboratory setup with appropriate coordinate frames is available in Fig. 10. The HITL experiments are conducted in the ZeroG lab with the Sun emulator as the only light source for increased fidelity in simulating the space environment.
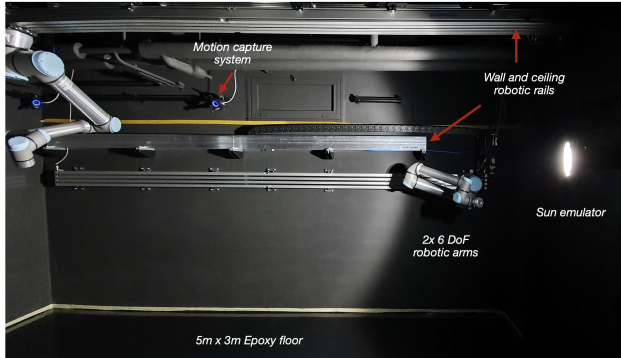

Figure 9: The Zero-G lab facility at University of Luxembourg [49]
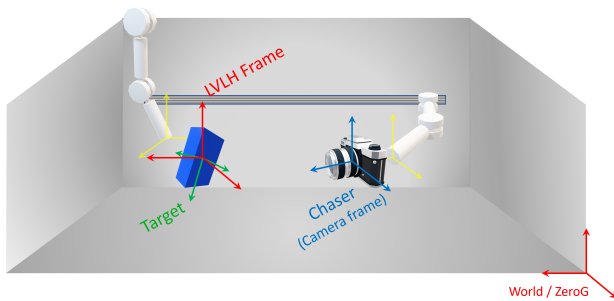
Figure 10: Schematic of laboratory setup with associated coordinate frames.

7.2. Robot Control

The ROS toolkit is an open-source robotics middleware used to control and communicate with the robots throughout the experimental setup. The computers are connected over the network running the robots, and the pose-estimation and the orbital dynamics simulations are pre-installed with ROS Melodic on a Linux-based operating system. Several processes run in the form of ROS nodes that communicate with each other to carry out hardware-in-the-loop simulations. ROS-visualization, RViz, is a ROS graphical interface that enables visualization of several ROS topics and assists in remote documentation and monitoring of the experiments. Robot motion is typically controlled using a method commonly referred to as "servoing" that uses feedback information from sensors such as a camera, OptiTrack motion capture systems, or a trajectory generator program (using externally available ROS topics), and streams the reference motion for the robot to follow. It is possible to provide the rendezvous path in the form of Cartesian set-points.

These paths are updated based on visual feedback and pose estimation run as separate ROS nodes, while servoing is performed to guide the chaser spacecraft to approach the target in the position space, as well as follow any changes in the orientation of the target. The motion of the target as realized by the robot is also realized via another servoing node running simultaneously with the chaser. Servoing is implemented via a modified implementation of MoveIt Servoing ROS package. MoveIt Servoing is a plugin in the MoveIt motion planning framework that allows for real-time control of robotic manipulators. It also consists of a set of ROS nodes that help in the pose-tracking of the robot using Cartesian motion set-points. Desired mockup position commands are directly streamed as inputs and the manipulator executes them concurrently. To get the existing system setup operating with MoveIt Servoing, the chaser and the target spacecraft mounted at the end of the UR10e flanges are also added as links to the xacro files and, therefore, made a part of the serial kinematic chain. The center of mass of each spacecraft is treated as the new tool-centre-point (TCP) of the robot. The following robot TCP is then treated as the command frame. The position way-points, obtained in the LVLH frame, are expressed in the command frame using appropriate transformations as set-points to the robot controller. Each spacecraft then follows its corresponding trajectory simulating rendezvous between the target and the chaser as closely as possible.

8. Results

The final approach phase between the chaser and the target is emphasized for evaluating the rendezvous operations in this investigation. When the separation between the chaser and the target is significantly large, the relative orientation between the two spacecraft is less pivotal. In such a case, the controller is inclined towards identifying an optimal trajectory for the chaser to progress toward the target spacecraft with little focus on matching the orientation. On the contrary, when the separation between the chaser and the target spacecraft is small, the determination of a rendezvous trajectory as well as maintaining appropriate relative orientation between the chaser and target spacecraft becomes equally crucial. Such a scenario becomes a criterion for testing and validating the control algorithm for rendezvous operations.

Analogous to the Gateway, the target spacecraft is contemplated to move along the 9:2 synodic resonant southern NRHO, particularly at apoapsis during the start of the approach. The target spacecraft experiences gravity torques exerted by the Earth and Moon, and tumbles under the dynamics. Such a complex scenario is deliberately selected to test the potency of the control algorithm while ensuring the chaser adapts to orbit and attitude changes proportionately. Two different tests are evaluated in this investigation: (1)

Table 3
Sample parameters for testing controller performance and hardware-in-the-loop (HITL) experiments.

Parameters	Case 1 (simulation)	Case 2 (simulation)	HITL (experiment)
Initial separation in LVLH frame ([x,y,z] m)	[-3.5, 1.5, 0]	[35,-15,-10]	[-0.80, 0.01, 0.04] (from actual observation)
Distance at rendezvous [m]	0.6	2	0.45
Collision avoidance distance [m]	0.6	2	0.45
Total time of propagation [hr]	4	3	3
Control segments	120	60	120
Max. control acceleration [m/s^2]	1.1×10^{-6}	2.7×10^{-5}	1.1×10^{-7}
Max. control torque per kg [Nm]	1.4×10^{-9}	7.0×10^{-8}	1.4×10^{-9}
$\mathbf{Q}_1$ [diagonal in $\log_{10}$ scale]	[3, 3, 3]	[0, 0, 0]	[1, 1, 1]
$\mathbf{Q}_2$ [diagonal in $\log_{10}$ scale]	[1, 1, 1]	[1, 1, 1]	[1, 1, 1]
$\mathbf{Q}_3$ [diagonal in $\log_{10}$ scale]	[0, 0, 0]	[0, 0, 0]	[0, 0, 0]
$\mathbf{R}$ [diagonal in $\log_{10}$ scale]	[−1, −1, −1, −2, −2, −2]	[0, 0, 0, −2, −2, −2]	[−1, −1, −1, −2, −2, −2]
Pose observation interval [s]	30	30	5
Errors in pose (3σ)	15 cm in x,y,z (absolute error) 0.03 in ϵ_i	10% in x,y,z (relative error) 0.03 in ϵ_i	NA (based on real pose values)
Incorrect orientation or pose flipping	1 in 30 observations	1 in 30 observations	NA (based on real pose values)

analyzing the capabilities of the controller based on simulation, and (2) hardware-in-the-loop (HITL) tests as a proof-of-concept for rendezvous in cislunar halo orbits with navigation using ArUco-markers-based optical sensing. Both the target and chaser spacecraft are modeled as uniform-density 6U CubeSats for both tests. The control algorithm is outlined with Object-oriented programming (OOP) in Python with standard libraries. The pose estimation algorithm is also programmed in Python using OpenCV library. These programs interface with the robotic manipulators over the Robot Operating System (ROS) network.

8.1. Controller Performance

The phase of the proximity operations is considered where the trajectory and orientation of the spacecraft are relevant. Of course, the control algorithm adapts to the varying distance of separation between the two spacecraft. Two distinct and diverse cases are evaluated. These cases are simulated with different parameters as listed in Table 3. In case 1, the chaser and the target spacecraft are initially separated by a distance of approximately 3.8 m and the entire rendezvous is expected to occur within 4 hours. For case 2 however, the initial separation is roughly 40 m, i.e., an order of magnitude higher than in case 1. Moreover, the proximity operations in case 2 happen within 3 hours; quicker than in case 1. Case 1 involves 120 equally-spaced discrete control inputs while only 60 control maneuvers are employed in case 2, over the entire course. The maximum values for the optimal control acceleration and torque are constrained to be within the values currently proposed for the Gateway mission [50]. Values for weighting matrices within the cost functional that guide the generation of optimal rendezvous path are as listed in Table 3 for both these cases.

Poor pose observation is detrimental to the control costs necessary to maintain the chaser spacecraft along the optimal rendezvous path. In practice, optical sensors on the chaser identify the pose of the target while it is itself in motion; certain poor pose observations may, therefore, be inevitable. The effects of uncertainties in pose identification on the quality of control are tested by introducing synthetic perturbations in the components of orbital motion and orientation. The resulting values of $\delta\mathbf{u}_k$ are monitored. For both cases, the frequency of observations is limited for availability only once every 30 seconds; further, 1 in every 30 observations is assumed to be pose flipped, i.e., supplying faulty orientation values. Besides, in case 1, the components of position along each direction are perturbed by an absolute 3σ value of 15 cm. On the contrary, a relative position error with 3σ of 10% along each of the three spatial directions is introduced in case 2. Finally, a perturbation of 3σ value of 0.03 along each component of the orientation quaternions is introduced for both cases. The results from the two cases are outlined as follows:

- Case 1. An optimal rendezvous path is determined with the approach site at 0.6 m from the center of the target, along the target body frame $\hat{i}_{[B]}$ axis; accordingly, the collision avoidance distance is established as 0.6 m. The optimal rendezvous path in configuration space is visualized relative to the [L] frame in Fig. 11. A snapshot of the two spacecraft at a certain time instant is also plotted to describe the mutual orientation of the two spacecraft during the approach. Figure 12 offers the actual path that incorporates linear control maneuvers once the synthetic pose errors are introduced. The optimal guidance path is also plotted for reference. A distinct difference between the actual

and optimal trajectory is not visible at a macro level in Fig. 12, primarily since the Kalman filter compensates for any large fluctuations in routine pose observations recorded along the process. A thorough inspection of the position coordinates in Fig. 13, however, yields a distinct difference between the reference rendezvous path (labeled by subscript 'ref'), the true path of spacecraft motion (labeled by subscript 'truth'), and finally the estimated path (labeled by subscript 'est'). Finally, the control history, both acceleration and torque, for cislunar rendezvous in case 1 are given in Fig. 14.
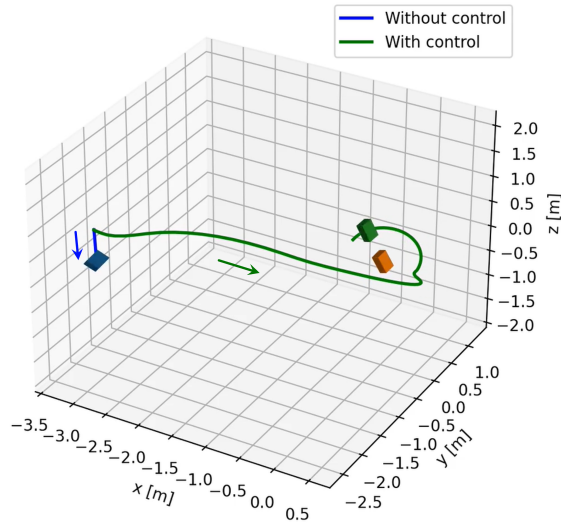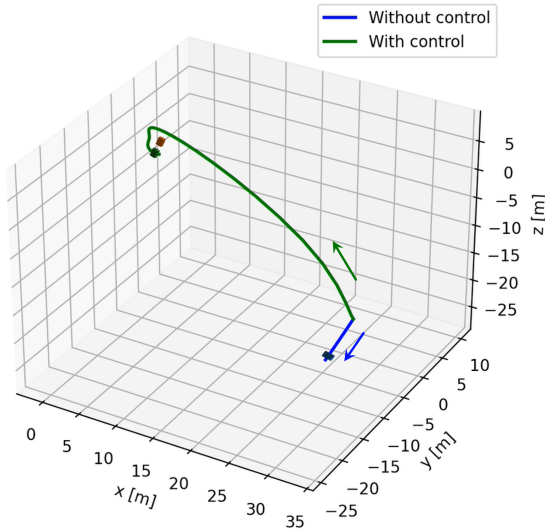

Figure 11: Optimal path for rendezvous, with a sample orientation of target and chaser spacecraft. Frame: LVLH. CubeSat scale: 2X. (Case 1)
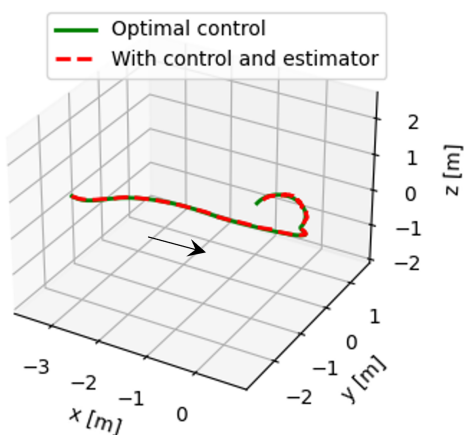
Figure 12: Actual rendezvous path for simulations with estimated poses. (Case 1)

- Case 2. Similar to the previous case, in case 2, a reference rendezvous path is determined such that the approach site is spaced 2 m from the center of the
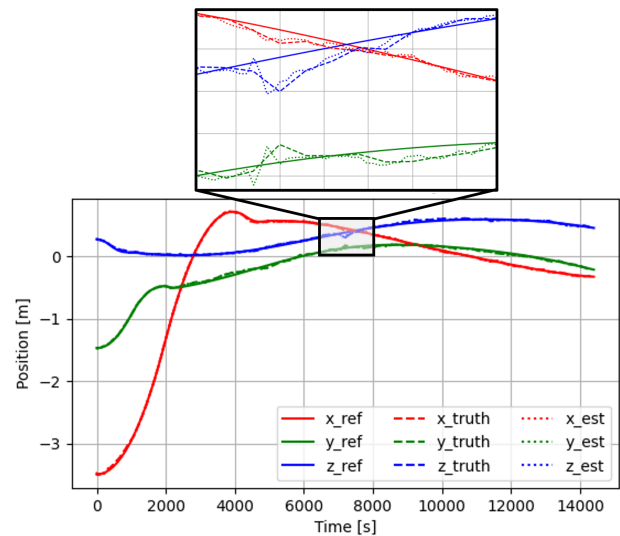
Figure 13: Position state history for the proximity operations. (Case 1)
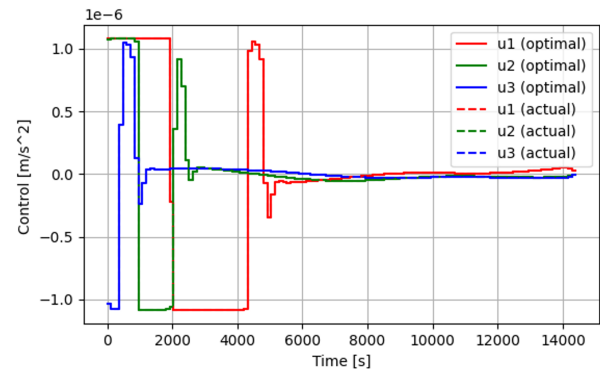
(a) Acceleration control history
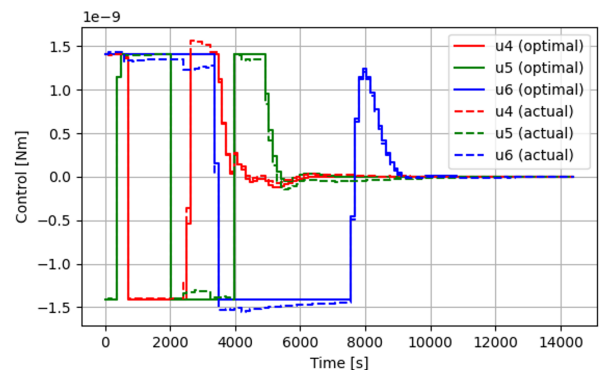
(b) Torque control history

Figure 14: Control history for rendezvous operations (Case 1). In certain regions, the optimal and actual control values have small differences and appear as overlapping.

target; consequently, the collision avoidance distance of 2 m is set. The optimal path along with a sample orientation of the target and chaser is demonstrated

in Fig. 15. Figure 16 illustrates the actual flight path given that perturbations from synthetic pose data are incorporated. Note that, in case 2, pose errors are relative while absolute 3σ pose errors are included in case 1. The overall geometry of the rendezvous path remains fairly consistent in configuration space despite uncertainties in the pose. Figure 17 offers the progression of the position states along the optimal reference path, the true path, and the estimated path. Figure 18 presents the acceleration and torque control history for case 2. In contrast to case 1, the maximum acceleration and torque level (along the reference path evaluated by nonlinear optimal control) is higher in case 2; the chaser thereby rapidly progresses toward the approach site near the target. Not surprisingly, the magnitude of the control costs, in consequence, are higher in the beginning and reduce substantially with time.

Figure 16: Actual rendezvous path for simulations with estimated poses. (Case 2)
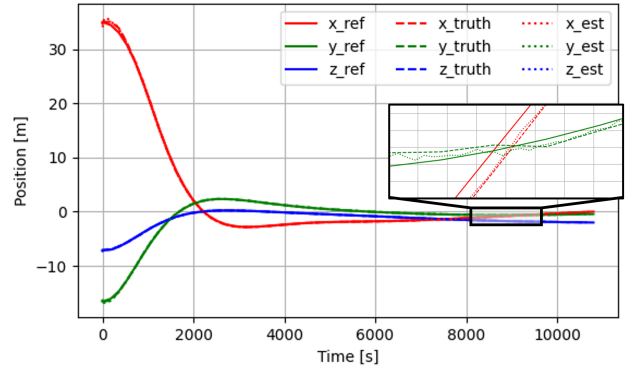
Figure 17: Position state history for the proximity operations. (Case 2)

Figure 15: Optimal path for rendezvous, with a sample orientation of target and chaser spacecraft. Frame: LVLH. CubeSat scale: 4X. (Case 2)

The quality of pose observations has a direct impact on the quality of the state estimation; a poor estimate triggers an increased deviation from the reference path. As a consequence, larger control costs are required to evolve near the desired rendezvous path. Frequent and precise pose observations are essential for improving efficiency and reducing the costs of corrective maneuvers.

8.2. Hardware-in-the-loop tests

The autonomy of the control algorithm for rendezvous operations is validated using hardware-in-the-loop tests. These tests are proof-of-concept for guidance and control strategies leveraging optical navigation techniques. Such autonomy presents potential opportunities in cislunar missions.
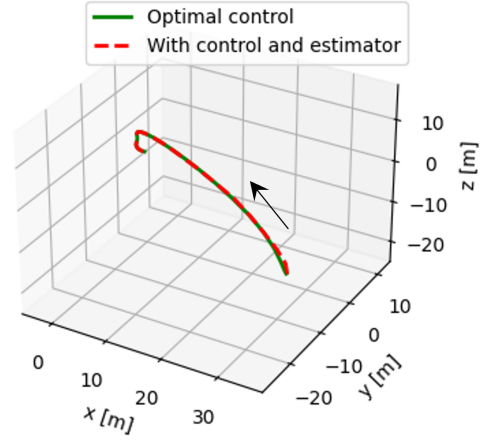
The guidance, navigation and control (GNC) techniques are validated in a sophisticated test facility.

8.2.1. Hardware and software integration

The ROS network offers a platform to integrate and communicate between hardware and software. As a language-agnostic tool, components programmed in different programming languages can send and receive information with very low latency over the ROS network. For the rendezvous operations in this investigation, a "Cislunar" ROS node serves as the leading piece of the entire hardware-in-the-loop architecture. It undergoes three primary tasks as follows:

1. Foremost, the node subscribes to the pose values for the target spacecraft relative to the chaser camera frame as well as the location of the chaser body relative in the laboratory space. For convenience, all the pose values are retrieved in the LVLH frame. Note that in common terminology, these packets of information are denoted as ROS topics. In this investigation, these information packages are communicated form of "geometry messages" which include Frame ID, the
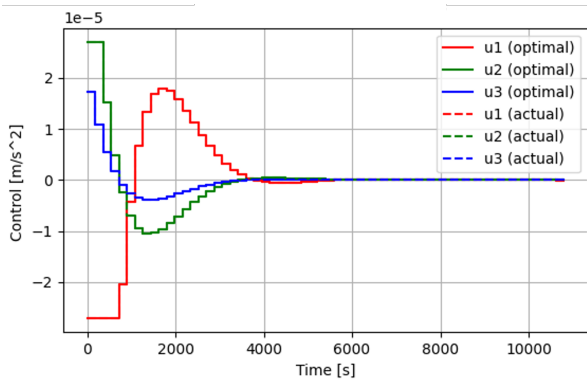
(a) Acceleration control history
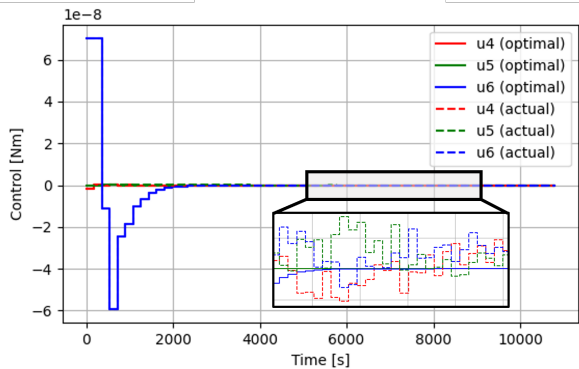
(b) Torque control history

Figure 18: Control history for rendezvous operations (Case 2). In certain regions, the optimal and actual control values have small differences and appear as overlapping.

time stamp of the message, position coordinates and orientation quaternions.

2. The node further includes the python controller package that apprehends the pose values to deliver maneuvers. At the initial time, the nonlinear controller within the package determines an appropriate cost-optimal reference path that is ideal for rendezvous. For any following observations, the package uses the available observation to update the state estimate and covariance. At certain time intervals, the algorithm also computes intermittent corrective maneuvers as necessary.

3. Finally, the node publishes the way-points, again in the form of position coordinates and orientation quaternions for both target and chaser spacecraft, that the robot is expected to follow. The way-points are also in the form of "geometry messages" that are published as ROS topics.

A simplified representation of the ROS node is presented in Fig. 19, indicating the subscribing and publishing topics. Further, Fig. 20 presents RViz with the actual robot configuration, visual feedback from the camera with the detection of ArUco markers on the target spacecraft, and visualization of the static transformations.

8.2.2. Test results

Numerical simulations in Cases 1 and 2 demonstrate the adaptability of the control algorithm for a range of motion. Such motion although plausible in the real world, the experimental rendezvous path is constrained to lie within the limited workspace accessible to the robotic arms as well as the marker detection distance for the camera. Initial conditions for the proximity operations are identified from the pre-existing configuration of both the robotic arms within their accessible workspace; an initial separation of approximately 0.8 m was determined. The relative pose of the target spacecraft is determined and an optimal path is calculated; the one determined in the experiment for a rendezvous duration of 3 hours is plotted in Fig. 21. A sequence of 120 control segments are, thus, placed at segment intervals of 90 seconds. Pose observations are recorded once every 5 seconds. Initial conditions and parameters used for the HITL tests are listed in Table 3.

The results from the hardware-in-the-loop tests are contemplated as follows:

- Filtering pose observations. The Kalman filter includes an inherent assumption that the noise is nearly Gaussian, however, such assumptions may not precisely hold with real-time pose observations. Further, the quality of the observations depends on several factors such as changing lighting conditions, the direction of the optical camera, the separation distance between the chaser and target, and even vibrations from the setup. Further determination of the pose of a moving target while the chaser itself is in motion may also generate uncertainties. Figure 22 displays the actual pose observations along with the estimate, reference, and true flight path at two sample locations. The nature of pose observations is different at these two locations, and may again vary at other locations. Some oscillations occur at a frequency of the maneuver delivery potentially due to the hardware setup, nevertheless, the amplitude of the observed vibrations is minuscule and handled conveniently by the Kalman filter. In general, pose observations are retrieved at significantly higher frequencies enabling an acceptable precision in state estimation. Figure 23 offers the history of the estimated flight path along with the true flight path and the reference path. A reasonable precision in the determination of the entire flight path is achieved with the Kalman filter working in tandem with the linear feedback controller. The actual flight path, one that incorporates observations and corrective maneuvers, is plotted along with the reference rendezvous path in the 3-dimensional configuration space in Fig. 24.

- Control costs. Optimal maneuvers are planned to follow the reference path ideal for rendezvous. The actual maneuvers, however, are the sum of the optimal and corrective maneuvers. The control history for the HITL test is presented in Fig. 25 for the optimal and actual maneuvers. A zoomed-in view is also available
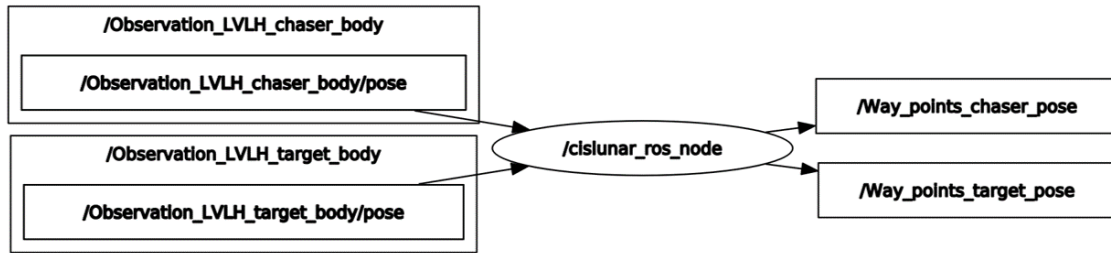
Figure 19: "Cislunar" ROS node to receive pose observations and communicate way-points for robot end-effectors to emulate the motion of the target and chaser spacecraft.
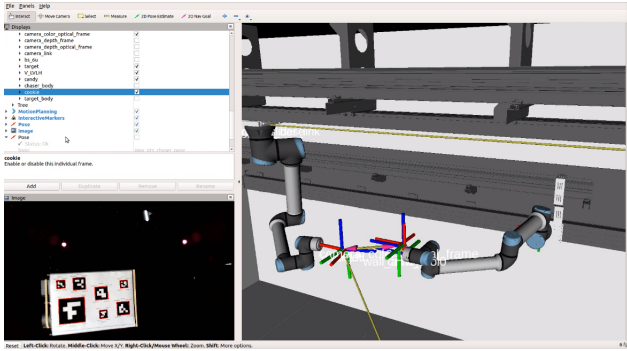

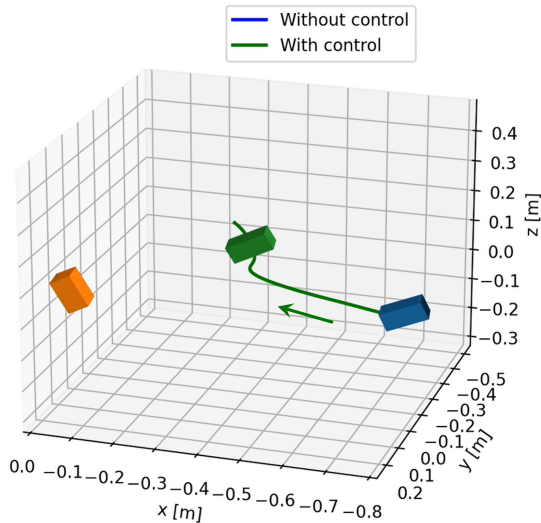**Figure 20:** Robot motion planning interface as visualized on RViz toolkit.

Figure 21: Optimal path for rendezvous, determined for HITL experiments. Frame: LVLH. Target is colored orange. CubeSat scale: 0.6X. Trajectory without control is visually obscured by the chaser body.

in Fig. 25b that distinctly reveals the evolution of corrective maneuvers while compensating the orientation errors. Despite these fluctuations, the chaser is able to rendezvous with the target in the neighborhood of the determined reference path.

- Computational time. The computational time to identify the optimal baseline rendezvous path after acquiring the initial pose along with system linearization near this baseline is approximately 200 to 400 seconds, depending on the case and the operating machines. In any flagship mission, a reference path is ideally known, hence, such a computational time is not translated during the actual flight. The routine computation of the corrective maneuver is, however, translated during actual flight operations. The "Cislunar" ROS node was able to operate at a frequency up to 6 Hz, i.e., subscribe to the pose data and publish relevant way-points for the spacecraft, roughly 6 times a second. The pose identification occurs significantly faster than the controller, up to 20 Hz; a pose is almost instantaneously available for subscribing. For the particular HITL case, pose observations are recorded at every 5 seconds of flight time, i.e., 0.2 Hz (indicated in Table 3), i.e., a total of 2160 pose observations in 3 hours of rendezvous time. At a frequency of operation at 6 Hz, the entire rendezvous operation may be emulated as fast as 6 mins ($= 2160/6 = 360$ s) in the laboratory. In practice, discrete maneuvers are not typically updated every 6 Hz. Perhaps 6 Hz is the limiting case and offers the maximum operational speed of the control algorithm. Modern pose estimation algorithms for space applications are capable of delivering poses at a frequency greater than 5 Hz [18, 19]. Since maneuvers are updated at a significantly lower frequency, the entire rendezvous operation is achievable in the real world.

The experiments are successful only with proper integration of software and hardware components. Figure 26 presents evidence and offers a direct comparison between the motion rendered by the robotic manipulators while emulating the spacecraft motion with the desired way-points visualized in RViz. The functionality of the control algorithm to perform in sync with the pose estimation algorithm and robotic manipulators (for emulating actual spacecraft trajectory) is validated with the HITL tests. Furthermore, real-time pose estimation for spacecraft navigation presents opportunities for precise rendezvous. Improved algorithms for a wider range of pose estimation scenarios potentially
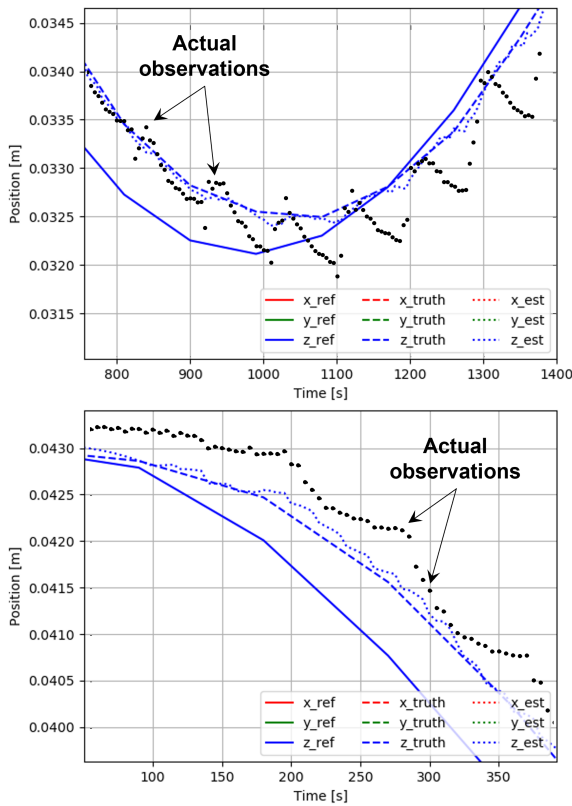
Figure 22: Actual state observations along with estimated values, true values and reference state values determined during HITL experiments. Zoomed-in view at two sample locations in $z_{[L]}$ direction.
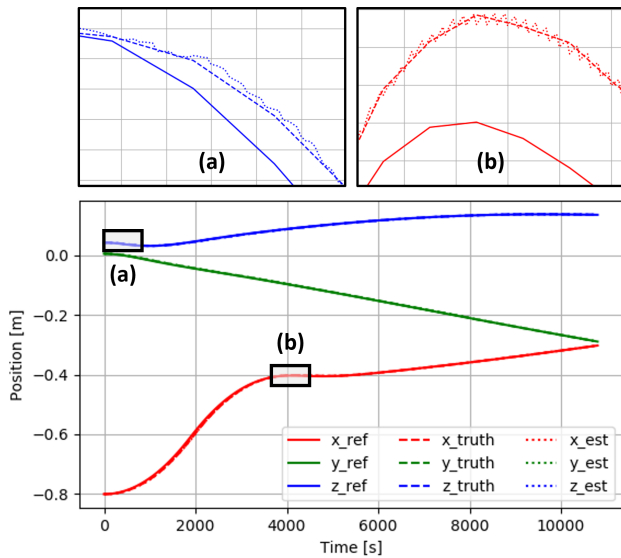

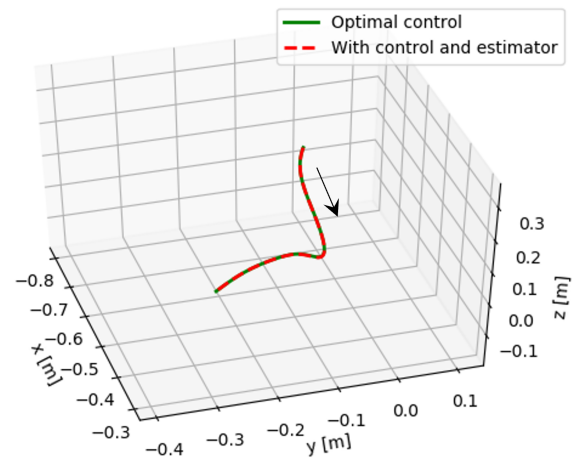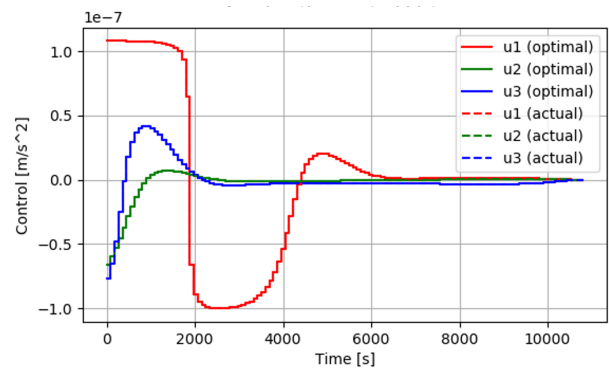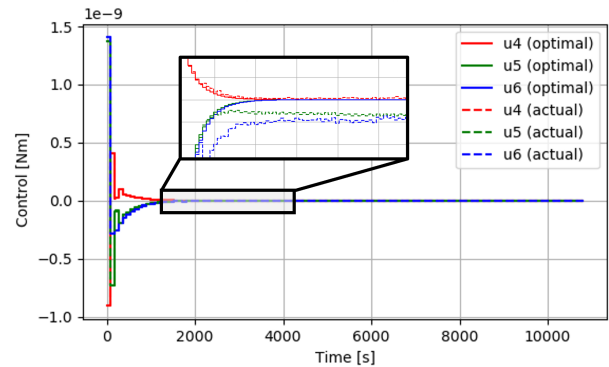**Figure 23:** Position state history for the HITL experiments

Figure 24: Actual rendezvous path with estimated poses, determined for HITL experiments.

(a) Acceleration control history

(b) Torque control history

Figure 25: Control history for experimental rendezvous operations

9. Concluding Remarks

A GNC technique for autonomous rendezvous operations in cislunar halo orbits is presented in this investigation, one that adopts a two-layered guidance and control approach. Firstly, the guidance algorithm using a nonlinear optimizer offers a baseline rendezvous path that accommodates both orbit and attitude motion for the chaser and target spacecraft
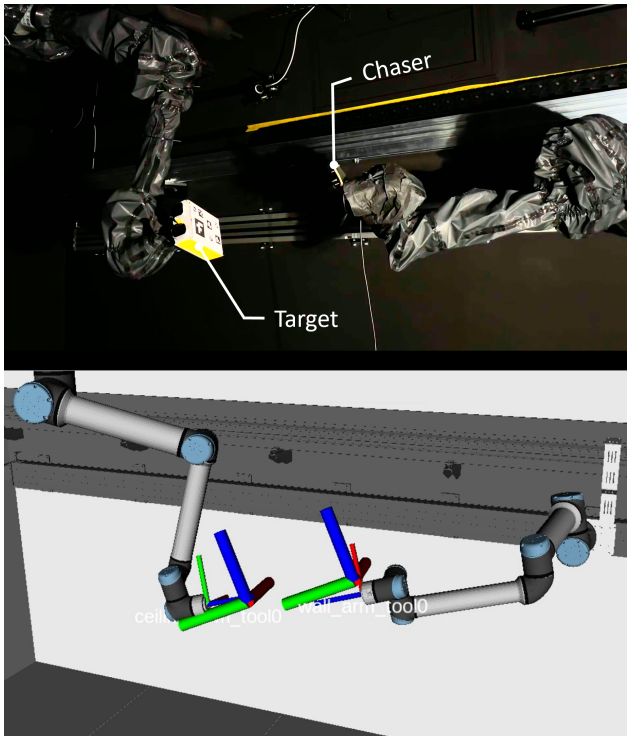
overcome the existing challenge of a limited operating distance of separation between spacecraft.

Figure 26: Robotic manipulators with target and chaser mock-ups (with its coordinate frames) as seen on RViz (bottom) vs configuration in laboratory space (top). The body frame axes $(\hat{x}, \hat{y}, \hat{z})$ for the target and chaser spacecraft are displayed in RViz with standard Red-Green-Blue (RGB) color format (bold).

in the circular restricted three-body problem. Subsequently, the linear controller compensates for any deviations identified from the desired baseline path, while incorporating feedback from optical navigation techniques. Vision-based navigation offers pose observations in this investigation. The designed algorithm is capable of performing rendezvous with a wide range of separations between the two spacecraft; two distinct cases are presented to validate this ability. Weighting matrices for the cost functional are altered on a case-by-case basis. From an operational perspective, the computationally intensive process of baseline generation may be performed on the ground, and gains required for the linear controller may be passed onto onboard computers.

A proof-of-concept autonomous GNC technique is elaborated with hardware-in-the-loop experiments. Spacecraft mockups on the end-effector of the two robots emulate the motion of the chaser and target for rendezvous in a Near Rectilinear Halo Orbit. Fluctuations in actual pose data are not precisely Gaussian, yet frequent real-time pose observations, processed through a Kalman filter, yield state estimates with reliable precision; therefore adequate for delivering corrective maneuvers. Pose estimation and controller communicate over the ROS network with low latency. In this investigation, the controller was able to operate at a frequency of as much as 6 Hz, much faster than the operational requirement.

Correspondingly, a real-world rendezvous application with a control frequency significantly less than 6 Hz is achievable. Ample time for capturing multiple pose data allows precise state estimation, resulting in the superior quality of control maneuvers.

The favorable outcome from the hardware-in-the-loop experiment further presents opportunities for more rigorous testing; particularly, evaluating long-range pose estimation algorithms, challenging lighting conditions, and an enhanced range of robot motion to emulate a spacecraft trajectory. The advancements in the GNC algorithm, one that incorporates an onboard optical navigation system, to actively undergo rendezvous operations enable exploitation of such activities in regions that are inaccessible directly from the Earth, for example, in the Earth shadow region (away from the line of sight). Such techniques further reinforce the potential to execute rendezvous in deep space, significantly farther from Earth.

Supplementary Materials

Supplementary material related to this article can be found online at https://doi.org/10.1016/j.actaastro.2023.06.028. A media demonstration of the hardware-in-the-loop test is presented.

References

[1] Nathan L Parrish, Matthew J Bolliger, Ethan Kayser, Michael R Thompson, Jeffrey S Parker, Bradley W Cheetham, Diane C Davis, and Daniel J Sweeney. Near rectilinear halo orbit determination with simulated DSN observations. In *AIAA Scitech 2020 Forum, Orlando, Florida, U.S.A.*, 2020.

[2] Sean Fuller, Emma Lehnhardt, Christina Zaid, and Kate Halloran. Gateway program status and overview. *Journal of Space Safety Engineering*, 9(4):625–628, 2022.

[3] Jason Crusan, Jacob Bleacher, Joe Caram, Douglas Craig, Kandyce Goodliff, Nicole Herrmann, Erin Mahoney, and Marshall Smith. Nasa's gateway: an update on progress and plans for extending human presence to cislunar space. In *2019 IEEE Aerospace Conference*, pages 1–19. IEEE, 2019.

[4] Davide Guzzetti and Kathleen C Howell. Coupled orbit-attitude dynamics in the three-body problem: A family of orbit-attitude periodic solutions. In *AIAA/AAS Astrodynamics Specialist Conference, San Diego, California, USA*, 2014.

[5] Davide Guzzetti and Kathleen Connor Howell. Attitude dynamics in the circular restricted three-body problem. *Astrodynamics*, 2(2):87–119, 2018.

[6] Giordana Bucchioni and Mario Innocenti. Rendezvous in cislunar space near rectilinear halo orbit: Dynamics and control issues. *Aerospace*, 8(3):68, 2021.

[7] Fouad Khoury and Kathleen C Howell. Orbital rendezvous and spacecraft loitering in the earth-moon system. In *AAS/AIAA Astrodynamics Specialist Conference, Lake Tahoe, California, USA*, 2020.

[8] Vivek Muralidharan, Carol Martinez Luna, Augustinas Zinys, Marius Klimavicius, and Miguel Angel Olivares Mendez. Autonomous control for satellite rendezvous in near-earth orbits. In *International Conference on Control, Automation and Diagnosis (ICCAD'22), Lisbon, Portugal*. IEEE, 2022.

[9] Vivek Muralidharan, Avishai Weiss, and Uros V Kalabic. Control Strategy for Long-Term Station-Keeping on Near-Rectilinear Halo Orbits. In *30th AIAA/AAS Space Flight Mechanics Meeting, Orlando, FL, USA*, January 2020.

[10] Andrea Colagrossi, Vincenzo Pesce, Lorenzo Bucci, Francesco Colombi, and Michèle Lavagna. Guidance, navigation and control for 6dof rendezvous in cislunar multi-body environment. *Aerospace Science and Technology*, 114:106751, 2021.

[11] Stéphanie Lizy-Destrez. Rendez vous optimization with an inhabited space station at eml2. In *Proceedings of 25th International Symposium on Space Flight Dynamics ISSFD 2015*, pages 1–17, Munich, Germany, October 2015.

[12] Naomi Murakami, Satoshi Ueda, Toshinori Ikenaga, Maki Maeda, Toru Yamamoto, and Hitoshi Ikeda. Practical rendezvous scenario for transportation missions to cis-lunar station in earth-moon L2 halo orbit. In *Proceedings of the 25th International Symposium on Space Flight Dynamics (ISSFD), Munich, Germany*, 2015.

[13] Yuki Sato, Kenji Kitamura, and Takeya Shima. Spacecraft rendezvous utilizing invariant manifolds for a halo orbit. *Transactions of the Japan Society for Aeronautical and Space Sciences*, 58(5):261–269, 2015.

[14] Yijun Lian, Yunhe Meng, Guojian Tang, and Luhua Liu. Constant-thrust glideslope guidance algorithm for time-fixed rendezvous in real halo orbit. *Acta Astronautica*, 79:241–252, 2012.

[15] Emmanuel Blazquez, Laurent Beauregard, Stéphanie Lizy-Destrez, Finn Ankersen, and Francesco Capolupo. Rendezvous design in a cislunar near rectilinear halo orbit. *The Aeronautical Journal*, 124(1276):821–837, 2020.

[16] Vivek Muralidharan, Mohatashem Reyaz Makhdoomi, Kuldeep Rambhai Barad, Lina Maria Amaya Mejia, Kathleen C Howell, Carol Martinez Luna, and Miguel Angel Olivares Mendez. Hardware-in-the-loop proximity operations in cislunar space. In *Proceedings of the International Astronautical Congress*, 2022.

[17] Francesco Colombi. Characterization of relative 6DOF natural and controlled dynamics in cislunar space. Master's thesis, Politecnico di Milano, 2019.

[18] Kevin Black, Shrivu Shankar, Daniel Fonseka, Jacob Deutsch, Abhimanyu Dhir, and Maruthi R Akella. Real-time, flight-ready, non-cooperative spacecraft pose estimation using monocular imagery. *arXiv preprint arXiv:2101.09553*, 2021.

[19] Dianqi Sun, Liang Hu, Huixian Duan, and Haodong Pei. Relative pose estimation of non-cooperative space targets using a tof camera. *Remote Sensing*, 14(23):6100, 2022.

[20] Claudio Vela, Giancarmine Fasano, and Roberto Opromolla. Pose determination of passively cooperative spacecraft in close proximity using a monocular camera and aruco markers. *Acta Astronautica*, 201:22–38, 2022.

[21] Xiaodong Du, Bin Liang, Wenfu Xu, and Yue Qiu. Pose measurement of large non-cooperative satellite based on collaborative cameras. *Acta Astronautica*, 68(11-12):2047–2065, 2011.

[22] Michel Bondy, Rubakumar Krishnasamy, Derry Crymble, and Piotr Jasiobedzki. Space vision marker system (svms). In *AIAA SPACE 2007 Conference & Exposition*, page 6185, 2007.

[23] L Pasqualetto Cassinis, Alessandra Menicucci, Eberhard Gill, Ingo Ahrns, and J Gil Fernandez. On-ground validation of a cnn-based monocular pose estimation system for uncooperative spacecraft. In *8th European Conference on Space Debris*, volume 8, 2021.

[24] Heike Benninghoff, Florian Rems, Eicke-Alexander Risse, and Christian Mietner. European proximity operations simulator 2.0 (epos)-a robotic-based rendezvous and docking simulator. *Journal of large-scale research facilities (JLSRF)*, 2017.

[25] Tae Ha Park, Juergen Bosse, and Simone D'Amico. Robotic testbed for rendezvous and optical navigation: Multi-source calibration and machine learning use cases. *arXiv preprint arXiv:2108.05529*, 2021.

[26] Heike Benninghoff, Toralf Boge, and Tristan Tzschichholz. Hardware-in-the-loop rendezvous simulation involving an autonomous guidance, navigation and control system. In *IAA Conference on Dynamics and Control of Space Systems, Porto, Portugal*, 2012.

[27] Vivek Muralidharan. *Stretching Directions in Cislunar Space: Stationkeeping and an Application to Transfer Trajectory Design*. PhD thesis, Purdue University, 2021.

[28] Victor Szebehely. Theory of orbits: the restricted problem of three bodies. Technical report, Yale University, New Haven, Connecticut, USA, 1967.

[29] Vivek Muralidharan and Kathleen C. Howell. Leveraging stretching directions for stationkeeping in earth-moon halo orbits. *Advances in Space Research*, 69(1):620–646, 2022.

[30] Chongrui Du, Olga L Starinova, and Ya Liu. Low-thrust transfer dynamics and control between halo orbits in the earth-moon system by means of invariant manifold. *IEEE Transactions on Aerospace and Electronic Systems*, 2022.

[31] Kathleen Connor Howell. Three-dimensional, periodic, 'halo' orbits. *Celestial mechanics*, 32(1):53–71, 1984.

[32] Emily M Zimovan-Spreen, Kathleen C Howell, and Diane C Davis. Near rectilinear halo orbits and nearby higher-period dynamical structures: orbital stability and resonance properties. *Celestial Mechanics and Dynamical Astronomy*, 132(5):28, 2020.

[33] Vivek Muralidharan and Kathleen C Howell. Stretching directions in cislunar space: Applications for departures and transfer design. *Astrodynamics*, 7(2):153–178, 2023.

[34] James R Wertz and Robert Bell. Autonomous rendezvous and docking technologies: status and prospects. *Space Systems Technology and Operations*, 5088:20–30, 2003.

[35] Giovanni Franzini and Mario Innocenti. Relative motion equations in the local-vertical local-horizon frame for rendezvous in lunar orbits. In *AAS/AIAA Astrodynamics Specialist Conference, Stevenson, WA, USA*, 2017.

[36] Joel A E Andersson, Joris Gillis, Greg Horn, James B Rawlings, and Moritz Diehl. CasADi – A software framework for nonlinear optimization and optimal control. *Mathematical Programming Computation*, 11(1):1–36, 2019.

[37] Lorenzo Pasqualetto Cassinis, Robert Fonod, and Eberhard Gill. Review of the robustness and applicability of monocular pose estimation systems for relative navigation with an uncooperative spacecraft. *Progress in Aerospace Sciences*, 110:100548, 2019.

[38] Roberto Opromolla, Giancarmine Fasano, Giancarlo Rufino, and Michele Grassi. A review of cooperative and uncooperative spacecraft pose determination techniques for close-proximity operations. *Progress in Aerospace Sciences*, 93:53–72, 2017.

[39] Sergio Garrido-Jurado, Rafael Muñoz-Salinas, Francisco José Madrid-Cuevas, and Manuel Jesús Marín-Jiménez. Automatic generation and detection of highly reliable fiducial markers under occlusion. *Pattern Recognit.*, 47(6):2280–2292, 2014.

[40] Francisco J. Romero Ramírez, Rafael Muñoz-Salinas, and Rafael Medina Carnicer. Speeded up detection of squared fiducial markers. *Image Vis. Comput.*, 76:38–47, 2018.

[41] Sergio Garrido-Jurado, Rafael Muñoz-Salinas, Francisco José Madrid-Cuevas, and Rafael Medina Carnicer. Generation of fiducial marker dictionaries using mixed integer linear programming. *Pattern Recognit.*, 51:481–491, 2016.

[42] G. Schweighofer and A. Pinz. Robust pose estimation from a planar target. *IEEE Transactions on Pattern Analysis and Machine Intelligence*, 28(12):2024–2030, 2006.

[43] Vincent Lepetit, Francesc Moreno-Noguer, and Pascal Fua. Epnp: An accurate o(n) solution to the pnp problem. *International Journal Of Computer Vision*, 81:155–166, 2009.

[44] M. Fischler and R. Bolles. Random sample consensus: A paradigm for model fitting with applications to image analysis and automated cartography. *Communications of the Association for Computing Machinery (ACM)*, 24(6):381–395, 1981.

[45] Oliver Montenbruck, Eberhard Gill, and Fh Lutze. Satellite orbits: models, methods, and applications. *Appl. Mech. Rev.*, 55(2):B27–B28, 2002.

[46] Sundarapandian Vaidyanathan and Christos Volos. *Advances and applications in nonlinear control systems*, volume 635. Springer, 2016.

[47] R. F. Stengel. *Optimal Control and Estimation*. Courier Corporation, 1994.

[48] Vivek Muralidharan, Avishai Weiss, and Uros Kalabic. Tracking neighboring quasi-satellite orbits around Phobos. In *World Congress of the International Federation of Automatic Control (IFAC), Berlin, Germany*, page 14906–14911. Elsevier, 2020.

[49] Mohatashem Reyaz Makhdoomi, Vivek Muralidharan, Kuldeep R Barad, Juan Sandoval, Miguel Olivares-Mendez, and Carol Martinez. Emulating on-orbit interactions using forward dynamics based cartesian motion. *arXiv preprint arXiv:2209.15406*, 2022.

[50] Robert Pritchett, Kathleen C Howell, and David C Folta. Low-thrust trajectory design for a cislunar cubesat leveraging structures from the bicircular restricted four-body problem. In *International Astronautical Congress, Washington D.C., USA*, 2019.